Fabrication of large free-standing nanostructured zone plates for focusing a Bose-Einstein condensate

Espen Selfors

Master's Thesis in Nano Science

Supervisors: Professor Dr. Bodil Holst
Dr. Martin Møller Greve

University of Bergen

August 7, 2017

Abstract

Matter wave optics is a fascinating area of physics touching many scientific disciplines ranging from microscopy to high precision gravity measurements. One of the major recent breakthroughs was the realization in 1995 of a Bose-Einstein condensate of atoms - a perfectly coherent atom source. Bose-Einstein condensates have been studied intensely over the last couple of decades, but surprisingly little work has been done on manipulation of the condensates using their de Broglie wavelength.

The original aim of this thesis was to create a Fresnel zone plate for the first focusing of a Bose-Einstein condensate via the de Broglie wavelength. The zone plate design parameters were chosen to fit the experimental setup of Prof. Zeilinger in Vienna, currently one of the only setups in the world where this experiment can be carried out.

The original aim of the thesis has been fulfilled. A free-standing silicon nitride zone plate with a diameter of 5 mm, and a focal length of 60 cm for a wavelength of 100 nm has been successfully created, tested with laser light and is now ready for experiments in Vienna. The zone plate has 44 zones, a 2 mm central stop and the width of the outermost zone is 12 µm. To the best of our knowledge this zone plate has a diameter more than an order of magnitude larger than any zone plates previously created for the focusing of matter waves. The much larger wavelength of the Bose-Einstein condensate compared to previous experiments meant that previously used fabrication methods could not be applied and new methods had to be developed as part of this thesis.

Aluminium wet etching, dry-etching of SiO_2 and silicon nitride using only a PMMA mask and quantified wet-etching of silicon were all established for the first time at the UiB NanoStructures laboratory as part of this thesis.

Acknowledgments

I would like to thank my supervisor, Prof. Dr. Bodil Holst, for making all of this possible by giving me the opportunity to work at the UiB NanoStructures laboratory and entrusting me with this project. Your feedback and ideas have been invaluable for finishing this thesis.

A special thanks goes to my second supervisor Dr. Martin Møller Greve. Without you, this thesis would never be possible. Thank you for always being there whenever I came running to you with equipment issues, no matter the time or day, and for showing me the ins and outs of the laboratory while fixing it. Thank you for always taking my crazy ideas seriously and letting me try them out, our discussions have been integral to deciding the course of this thesis.

I would also like to thank the entire nanophysics group for all your assistance and your enlightening presentations. No matter the subject, your papers and presentations have always been fascinating, including the customary paper-cake. The trip to Voss was one of the highlights of a tough spring semester. Sondre Sandberg deserves a special acknowledgment for being a great office partner. Our conversations and breaks have kept me motivated throughout these two years.

Thank you to Roald Langøen at the in-house workshop for always being helpful, regardless of what project I brought to him.

I want to thank my family for being supportive and motivating at every possible moment, especially when I was buried in work.

I would like to thank my girlfriend Waldis Werdal for always believing in me, even when I did not. Your support and love is what has kept me going. Last but not least, I want to thank my son Vetle, for always brightening my day.

Contents

Abstract **i**

Acknowledgements **iii**

List of Figures **vi**

List of Tables **viii**

Abbreviations **ix**

1 Introduction **1**
1.1 Matter Wave Optics 1
1.1.1 Bose-Einstein Condensates 2
1.2 Thesis Objectives 3
1.3 Thesis Outline 4

2 Theory **5**
2.1 Zone Plate Equation 5
2.1.1 Zone Plate Resolution 8
2.2 Zone Plate Parameters 9

3 Fabrication Techniques **11**
3.1 Facilities 11
3.2 Electron Beam Lithography 12
3.2.1 Resist 12
3.2.2 Raith e-LiNE System 13
3.3 Electron Beam Evaporator 15
3.4 Reactive Ion Etching 17
3.5 Chemical etching 20
3.5.1 Aluminium Wet-Etching 20
3.5.2 Silicon Wet-Etching 20

4 Characterization Techniques **22**
4.1 Scanning Electron Microscopy 22
4.2 Optical Testing of Zone Plates 24

5 Methods **26**
5.1 Pattern Creation 26
5.2 Aluminium Zone Plate 28
5.2.1 Material Choices 28
5.2.2 Sample Holders 30
5.2.3 Pattern Transfer 30
5.3 Silicon Substrate Zone Plates 33
5.3.1 Silicon Membrane Fabrication 34
5.3.2 Silicon Zone Plate 36
5.3.3 Silicon Nitride Zone Plate 37
5.3.4 Chromium Zone Plate 38
5.4 Experimental Procedure 38
5.4.1 Resists 38
5.4.2 EBL Patterning 39
5.4.3 Pattern Transfer Reactive Ion Etch 40
5.4.4 Aluminium Wet-Etch 41
5.4.5 Silicon Wet-Etch 41
5.4.6 Chromium Zone Plate 42

6 Results and Discussion **43**
6.1 Reactive Ion Etching SiO_2 43
6.2 Aluminium 45
6.2.1 Etching Aluminium 45
6.2.2 Imaging Issues 49
6.3 Chromium Zone Plate 50
6.4 Reactive Ion Etching Silicon Nitride 51
6.5 Silicon Substrates 51
6.5.1 Silicon Membranes 51
6.5.2 Silicon Zone Plate 52
6.6 Successful Fabrication of a Silicon Nitride Zone Plate 60
6.6.1 Optical Measurements 66

7 Conclusions and Future Work **69**

Bibliography **70**

Appendix **77**

List of Figures

1.1 Experimental setup for trapping Bose-Einstein condensate . . 3
2.1 Zone plate construction 6
3.1 Raith e-LiNE system 14
3.2 Overview electron beam evaporation 16
3.3 Diagram of reactive ion etching chamber 17
4.1 Diagram of SEM+EBL system 23
4.2 Schematic optical testing of zone plates 24
5.1 ASCII code for pattern 27
5.2 Modifying pattern file 28
5.3 Cross section aluminium stack 29
5.4 Aluminium sample holder - bottom 31
5.5 Aluminium sample holder - top 32
5.6 Schematic silicon membrane 34
5.7 Etching of diagonal lines in KOH 37
6.1 Initial SiO_2 dry etching results 44
6.2 DC-bias vs. RF-power for SiO_2 dry-etch 44
6.3 Dry-etching SiO_2 with new recipe 45
6.4 Initial aluminium etch results 46
6.5 Attempted residue removal, aluminium 47
6.6 Aluminium etching after PMMA removal 47
6.7 Feature dependent etching of aluminium 48
6.8 Pattern splitting to match etch rates 49
6.9 Measured thickness Cr and PMMA 50
6.10 Optical micrograph of chromium zone plate 51
6.11 Dry-etching silicon nitride with PMMA mask 52
6.12 Depth measurements during silicon membrane fabrication . . . 53
6.13 Cross section of silicon membrane 54
6.14 Overview 5 µm deep pattern 55
6.15 3 µm deep pattern, outer zone 56
6.16 Overlapping zones due to angling 57
6.17 4 µm deep pattern in Si, overlapping zones 58

6.18 5 µm deep pattern in Si, parallel zones 58
6.19 Optical micrograph of backside - Overetched silicon zone plate 59
6.20 Top right quarter of silicon nitride zone plate 60
6.21 Support bar - silicon nitride zone plate 61
6.22 Details - support bar silicon nitride zone plate 62
6.23 350 µm Suspended silicon nitride 63
6.24 Zone plate thickness and reattaching nitride 63
6.25 Inner zones of factor 14 zone plate 64
6.26 Nitride zone plate using support factor 14 65
6.27 Intensity comparison nitride and chromium zone plate 67
6.28 Optical testing of nitride zone plate 68

List of Tables

2.1 Zone plate parameters 9
5.1 Masking material and etchant compability. 28
5.2 Etch rates Transene Aluminium etchant Type A 41

Abbreviations

Abbreviation	Explanation
SEM	Scanning electron microscope
SE	Secondary electrons
BEC	Bose-Einstein condensate
EBL	Electron beam lithography
PMMA	Poly(methyl methacrylate)
IPA	Isopropyl alcohol
RIE	Reactive ion etch
FWHM	Full width at half maximum

Chapter 1

Introduction

This chapter gives a short introduction to the field of matter waves and Bose-Einstein condensates including a brief description of state of the art for de Broglie diffractive optical elements, that is, optical elements that manipulate matter via its de Broglie wavelength. The chapter finishes with a formulation of the thesis goals.

1.1 Matter Wave Optics

In 1924 Louis de Broglie proposed in his PhD thesis that matter share the characteristics of light, it can behave as a wave and a particle, with a wavelength given by [1]

$$\lambda = \frac{h}{p} \tag{1.1}$$

where h is the Planck constant $6.626 \times 10^{-34}\mathrm{J\,s}$ and p is the momentum. This has later been experimentally verified on numerous occasions using for example electrons[2], atoms[3], large fullerenes[4] and large porphyrins with a mass of $10\,000\,\mathrm{u}$[5].

The discovery of the wave properties of matter enabled a completely new area of physics, namely matter wave optics. Early matter wave experiments utilized crystal surfaces[3] and single slits[6]. The development of modern nano-fabrication tools like electron beam lithography enabled the fabrication of complex structures for manipulating atoms and molecules. It should be mentioned that a whole branch of matter wave optics is dedicated to the manipulation of atoms and molecules using magnetic and electrostatic fields,

however, this will not be discussed further in this thesis.

One of the main projects of the UiB nanophysics group is the realization and implementation of a neutral helium microscope[7][8][9][10][11]. Helium microscopy opens up the possibility for non-destructive imaging of sample surfaces at 10 nm resolution. As the helium atoms are neutral, any sample can be imaged and one is not limited to using conductive samples.

A major challenge in the implementation of a helium-based microscope is focusing the helium beam. Early work used an aperture [12], but this is limited to low resolution and low intensities[13]. Fresnel zone plates have been used to focus a supersonic beam of helium down to 2 µm[13] and later to 1 µm[7]. The first images using neutral helium atoms was presented in 2008[14].

Electromagnetic focusing of neutral helium atoms is not viable due to low polarizability and lack of spin[13]. Another possible technique for focusing helium beams is the use of single crystal mirrors. In 1997 Holst and Allison successfully focused a beam of neutral helium atoms using an electrostatically bent crystal as a focusing mirror[15].

This avoids chromatic aberrations and has the added benefit of higher intensities than a Fresnel zone plate, where at least 90% of the incoming intensity is lost, see (2.10). However, while the resolution of Fresnel zone plates in matter wave optics is limited by chromatic aberrations, the resolution of mirrors are limited by the production methods. So far the spot sizes achieved using mirrors are still larger than 10 µm[16].

The main obstacle in producing the Fresnel zone plates for the helium microscope is the demand for free-standing elements. The lack of surface penetration is the reason why helium is chosen as a surface probe in the first place, this also extends to the optical elements.

1.1.1 Bose-Einstein Condensates

A standard molecular beam produced using supersonic expansion has a velocity spread of around 0.5%, however, it is now possible to produce a perfectly coherent molecular beam, with in principle no velocity distribution by making a so called Bose-Einstein condensate(BEC) and dropping it from a height. Of special interest for this thesis is the setup for Bose-Einstein condensate of metastable helium, made in the group of Prof. Zeilinger at the University of Vienna[17].

BEC is a state of matter consisting of atoms or small molecules, with integer spin, all in the same quantum state. This state occurs when the de Broglie wavelength of the particles becomes longer than the inter-particle

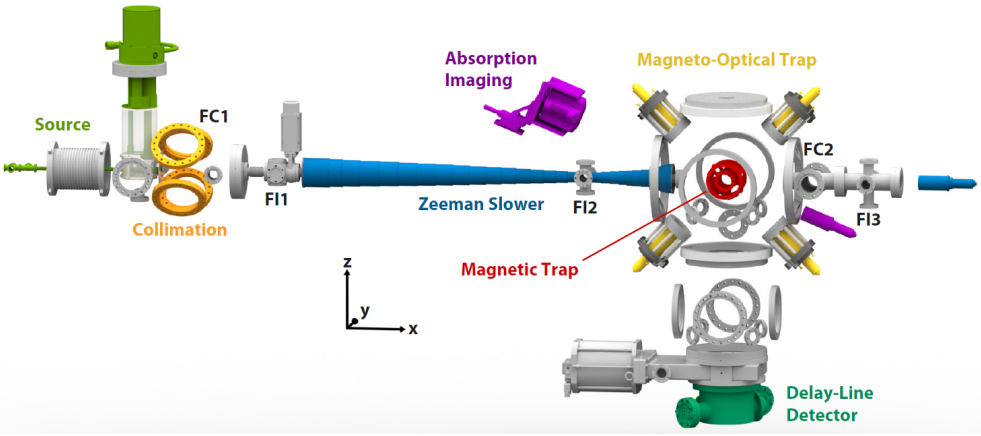

Figure 1.1: Overview of the setup used to create and detect the Bose-Einstein condensate by Keller et al. The zone plates would be placed between the Magneto-Optical Trap and the detector, focusing the BEC onto the detector. Image taken from [17].

separation, and the waves will overlap.

This requires a high density and low temperatures. Typically this is achieved by slowing down a beam of metastable helium using lasers before trapping it using a combination of magnetic fields and lasers. After being trapped, the atoms are further cooled by evaporative cooling, where a laser is used to remove the highest energy atoms, effectively cooling the remaining atoms. The final achieved temperature is about 1 µK.

The metastable helium is created by exciting the electrons of the helium to a high energy orbital, 2^3S_1. This energy state lies 20 eV above the ground state, close to the first ionization energy of 24.6 eV. 2^3S_1 is used because it is long-lived, with a lifetime of up to 8000 s[18]. The high energy also makes the atoms easier to detect, enabling detection of single atoms. For more information about the system and methods used, see the original article by Keller et al.[17]. An overview of the system is included in figure 1.1.

Judd et al. has done some theoretical considerations of using reflective and transparent Fresnel zone plates to focus Bose-Einstein condensates of alkali metals. They propose this as a technique for erasable lithography[19].

1.2 Thesis Objectives

- The main focus of this thesis is designing a process to fabricate large free- standing zone plates for making the first experiment on the focusing of a Bose-Einstein condensate via its de Broglie wavelength. More

specifically this means:

- Choose a suitable substrate-masking material pair that can be processed at the UiB NanoStructures laboratory.
- Establish methods and parameters required for manufacturing structures in the micrometer range.
- Fabricate zone plates with given parameters for large wavelength applications and characterize them using an optical setup as a substitute for matter waves.

1.3 Thesis Outline

Chapter 2 introduces the classical optics theory behind binary Fresnel zone plates and how this relates to matter waves. Chapter 3 describes the equipment and techniques used for the fabrication. Chapter 4 presents the characterization techniques used in the fabrication and imaging of the samples. Chapter 5 outlines the specific work done in this thesis and provide more information regarding the experimental procedure needed to replicate the results. Chapter 6 presents the results with discussion. Chapter 7 delivers the conclusions, advice for future work and possible alternative approaches.

Chapter 2

Theory

This chapter presents the theory of Fresnel zone plates. It gives a short introduction to the mechanism behind their function before deriving the shape necessary to tune the focal length. This is derived here for plane waves and point sources, but the incident Bose-Einstein condensate is assumed to be a perfect plane wave. This is only an approximation. There has been several theoretical papers discussing the exact wave nature of a Bose-Einstein condensate, however, this will not be discussed further in this thesis. Subsequently, the resolution of Fresnel zone plates is derived and the specific parameters used for the zone plates in this thesis are presented.

2.1 Zone Plate Equation

A Fresnel zone plate is an optical element relying on diffraction to bring waves to a focus. It consists of alternate opaque and transparent rings, zones, with radii tailored to create constructive interference at a given focal length.

For the simplest case consisting of plane wave illumination of wavelength λ on a zone plate with odd zones transparent, i.e. the first zone is blocked, the widths and radii of the zones can be determined using geometrical considerations. To achieve constructive interference, the path length from the zone plate to the focus can not differ by more than $\frac{\lambda}{2}$ within a zone. This means that

$$l - f < \frac{\lambda}{2} \tag{2.1}$$

define the first zone. Whether this zone is chosen as open or closed is arbitrary. For this work it is chosen as a closed zone. The second zone, kept

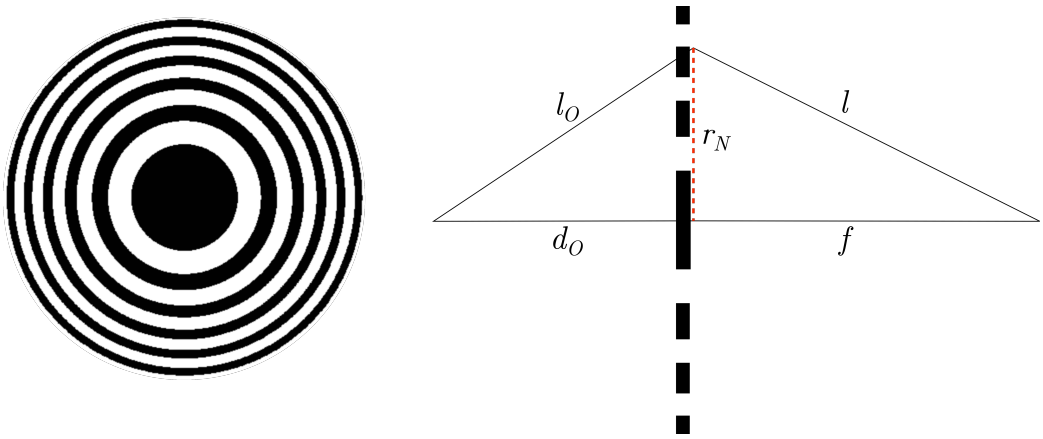

Figure 2.1: Left: Overview of a general Fresnel zone plate. Dark areas are opaque and white areas are transparent.
Right: Variables used to construct the zone plate equation. For a plane wave, $d_0 = \infty$

open, is then given by

$$\frac{\lambda}{2} < l - f < \lambda \tag{2.2}$$

where l and f is the path length to the focus from a point in the zone and focal length of the zone plate, respectively. The transition from the nth zone to the next is given as

$$l - f = \frac{n\lambda}{2} \tag{2.3}$$

which can be rewritten as

$$\sqrt{f^2 + r_n^2} - f = \frac{n\lambda}{2} \tag{2.4}$$

using Pythagoras. Solving this equation for r_n yields

$$r_n = \sqrt{n\lambda\left(\frac{n\lambda}{4} + f\right)} \tag{2.5}$$

For a point source situated a fixed distance d_o away from the zone plate, the path length to the focal spot is instead given as

$$(l_o - d_o) + (l - f) < \frac{\lambda}{2} \tag{2.6}$$

or equivalently to (2.4)

$$\left(\sqrt{d_o^2 + r_n^2} - d_o\right) + \left(\sqrt{f^2 + r_n^2} - f\right) = \frac{n\lambda}{2} \tag{2.7}$$

squaring this twice and solving for r_n gives[20]:

$$r_n^2 = \frac{n\lambda d_o f(d_o + f) + \frac{1}{4}(n\lambda)^2(d_o^2 + f^2 + 3d_o f) + \frac{1}{8}(n\lambda)^3(f + d_o) + \frac{1}{64}(n\lambda)^4}{\left(d_o + f + \frac{n\lambda}{2}\right)^2} \tag{2.8}$$

which, by assuming $n\lambda \ll (d_o + f)$, can be simplified by removing higher order terms. This results in a zone radius of

$$r_n = \sqrt{\frac{n\lambda d_o f}{d_o + f}} \tag{2.9}$$

If a zone plate is fabricated using this criteria, it will focus the waves from a point source situated d_o away from the zone plate to a point f away from the zone plate. For a large d_o and by ignoring higher order terms, (2.9) and (2.5) becomes equal.

The considerations so far have concentrated on the first order diffraction. Higher order, negative order and zero order diffraction will also occur. Higher order focal points will be found at distances $\frac{f}{3}$, $\frac{f}{5}$, $\frac{f}{7}$ and so on[21]. Even numbered diffraction orders correspond to total destructive interference and will not be visible. Negative order diffraction corresponds to virtual focal points, placed upstream from the zone plate, and hence results in a divergent beam.

A binary zone plate constructed using (2.5) or (2.9) will have a ratio of open to closed area of about 0.5, meaning 50% of the incident intensity will be transmitted. This 50% is further split into 25% in the 0-order, 10.1% for each of the 1st and -1st order and 1.1% each in the 3rd and -3rd order, given by[22]:

$$\eta = \left(\frac{\sin\left(\frac{a}{d}m\pi\right)}{m\pi}\right)^2 \tag{2.10}$$

where η is the transmittance for a given diffraction order, $\frac{a}{d}$ corresponds to the ratio of open to closed zones and m is the diffraction order. For the zone plates fabricated in this thesis this ratio is further reduced by the use of a large central stop and removal of parts of the pattern for support.

It is worth noting that the Raith program used to create the original

zone plate pattern in this thesis uses a free parameter of $\alpha = 0.25$ when creating the pattern, corresponding to a phase shift of 90° or $\frac{\pi}{2}$. This means that n in (2.5) is replaced by $(n - \alpha)$. This phase shift does not affect the focus because the shift is equal for each zone and the zone widths are not altered[23]. However, this will cause all zones to be closer to the center.

This chapter has considered a general wave. The wave may be light or matter waves of atoms or molecules, the same general considerations about diffraction applies. In this thesis, the zone plates are intended for focusing a Bose-Einstein condensate, explained in the previous chapter.

2.1.1 Zone Plate Resolution

The resolution of a zone plate is a measure of how small of a spot the beam can be focused to. A typical way of defining this is by the full width at half maximum (FWHM) of the focal spot, also called the Abbe criterion. The resolution is then given by

$$r = \frac{\lambda}{2\mathrm{NA}} \tag{2.11}$$

where λ is the incoming wavelength and NA is the numerical aperture of the zone plate. Numerical aperture is a measure of the angle of the beam leaving the zone plate at the outermost zone, given by $\mathrm{NA} = \sin\theta$. By looking at the outer zones as a diffraction grating, the numerical aperture can be found from the first order diffraction grating equation

$$\sin\theta = \frac{\lambda}{d} \tag{2.12}$$

where θ is the angle of the diffracted beam and d is the slit spacing. The slit spacing in this case will be approximately double the width of the outermost zone

$$d = 2r_N \tag{2.13}$$

This yields a numerical aperture of

$$\mathrm{NA} = \frac{\lambda}{2r_N} \tag{2.14}$$

Inserting this into (2.11) yields

$$r = \frac{\lambda}{2\left(\frac{\lambda}{2r_N}\right)} = r_N \tag{2.15}$$

The resolution, given by the FWHM, is then defined as the width of the outermost zone. The zone plates fabricated in this thesis has a resolution of 12 µm, while the detector used in the BEC setup currently has a resolution of 177±32 µm. The resolution is thus adequate for focusing the BEC to a single pixel for the first order focal point.

2.2 Zone Plate Parameters

Parameter	Value
Wavelength	100 nm
Focal length	600 mm
Diameter	5 mm
Diameter central stop	2 mm
Outermost zone width	12 µm

Table 2.1: Parameters used for the zone plate patterns.

The parameters used for fabricating the zone plates are shown in table 2.1. The wavelength is chosen to match the experiment in the group of Prof. Zeilinger. Using the specified values from [17], the density of the produced condensate, n, can be calculated as:

$$n = \frac{N}{V} = \frac{N}{\frac{4}{3}\pi R_{rad}^2 R_{ax}} = \frac{10^6}{\frac{4}{3}\pi \times (7\,\mu\text{m})^2 \times 140\,\mu\text{m}} \tag{2.16}$$

$$n = 3.5 \times 10^{19}\text{m}^{-3}$$

where N is the total number of atoms in the condensate, while R_{rad} and R_{ax} is the radii of the ellipsoidal condensate. The phase-space density is given by

$$\text{Phase space density} = n\lambda_{dB}^3 \tag{2.17}$$

with the measured phase space density being 0.1, this gives

$$\lambda_{dB} = \sqrt[3]{\frac{0.1}{n}} = 142\,\text{nm}$$

This is the de Broglie wavelength of the condensate before being released from the magnetic trap. The condensate will accelerate in the gravitational field, increasing momentum and thereby decreasing its de Broglie wavelength, see (1.1). This is a rough estimate of the wavelength and if the wavelength does not match the wavelength used for the pattern, the focal length will change. This means the zone plate may need to be closer or further away from the detector.

The original focal length was chosen to be 600 mm to match the 800 mm distance from the magnetic trap to the detector. A large central stop is included to avoid the zero order beam being close to the focal spot. A zone plate constructed according to (2.5) with the parameters from table 2.1 will have 44 total zones and a theoretical resolution of 12 µm.

Chapter 3

Fabrication Techniques

This chapter presents the fabrication techniques used during this work. It describes the facilities and the equipment used for electron beam lithography, dry-etching and electron beam evaporation. Finally the two wet etch processes are presented with theory and general considerations. The processes developed and implemented specifically for this thesis work have been described in more details.

3.1 Facilities

The experimental part of this thesis was carried out at the University of Bergen's NanoStructures laboratory. The laboratory consists of four main parts: ISO-5 cleanroom with airlock, semi-cleanroom, storage room and the room hosting the e-LiNE (electron - Lithography and NanoEngineering) tool. The semi-cleanroom contains the electron beam evaporator system, optical microscopes and a fume hood. Another fume hood is situated inside the ISO-5 clean room along with a spin coater, a reactive ion etching system and a thin film analyzer. The e-LiNE is situated in a temperature stabilized ISO-7 cleanroom cabin.

ISO-5 and ISO-7 are ISO 14644-1 classifications for cleanrooms. These classifications are based on the maximum number of particles larger than 0.1 µm per cubic meter of air, with ISO-5 containing the least amount of particles of the two[24]. This is achieved by have having filtered air enter the room through the roof and exciting along the floor, creating a positive pressure compared to outside the cleanroom. This forces particles towards to floor and out of the room. Another crucial part for minimizing airborne particles is the use of lab coats, hairnets and mouth covers by all personnel

inside the laboratory.

3.2 Electron Beam Lithography

Lithography is a method of transferring a pattern from one medium to another. In electron beam lithography (EBL) this is achieved by scanning a beam of electrons over a sample coated with an electron-sensitive material, a resist. This resist will undergo physical and/or chemical changes where it has been exposed to the beam and a pattern can be created. The use of a highly focused beam enables the creation of patterns with nanometer resolution. EBL differs from photolithography in that it is a maskless process. This allows for the pattern to be freely adjusted between each exposure, in contrast to conventional lithography techniques where a pre-made mask is used. Another advantage of EBL over photolithography is that it is not limited by diffraction. The de Broglie wavelength of electrons used is <1 Å. The main disadvantage of EBL is the low throughput. The beam needs to be scanned over the area to be exposed, step by step. This leads to write times of several hours for larger patterns. The write time is determined by several factors, mainly beam current, resist thickness and desired resolution. EBL is thus mostly a technique for research and applications where a large throughput is not necessary.

3.2.1 Resist

Poly(methyl methacrylate), PMMA, is the most common resist used for EBL[25] and is the resist used throughout this thesis. It is also the standard resist used at the UiB NanoStructures laboratory. In the context of its use as a photo- or e-beam-resist it consists of varying length polymer chains dissolved in methoxybenzene, chlorobenzene or ethyl acetate. Commercially available PMMA for EBL has chains with a molecular weigth of 50 000-2 200 000 g/mol (50k-2 200k). Typically chains of size 496k and 950k are used in EBL[25]. To apply a thin uniform layer, the samples are spin coated and subsequently baked on a hot plate to remove the solvent. Final thickness of the layer will depend on chain length, ratio of PMMA/solvent and the rotational speed used for spin coating. Larger chains and higher PMMA content will increase viscosity of the solution, leading to thicker films.

When the chains in PMMA are exposed to electrons in the beam they will undergo depolymerization and be cleaved into smaller radical chain fragments[26]. Radical fragments from a 950k PMMA are mainly in the 0.1-1k

range, 1-10 monomers in in size[27]. Solubility of PMMA increases with decreasing chain size and the PMMA can subsequently be removed from the exposed regions with an appropriate developer.

PMMA is a mainly used as a positive tone resist, i.e. the exposed area will be removed. However, if PMMA is overexposed, a larger number of radical fragments will be created and they will undergo crosslinking. This leads to recombination of fragments and chains larger than the original 950k chains. When this happens, PMMA will be *less* soluble where exposed. PMMA can then be used as a negative tone resist, although this requires a very large dose, hence it is time consuming. It is however worth noting that this may create hard to remove PMMA on samples if imaged for too long in the SEM. Dedicated negative resists are available, like hydrogen silsesquioxane (HSQ). Another noteworthy positive resist is ZEP520, which has a higher sensitivity and etch resistance than PMMA[28].

The required dose for a resist is a measure of how many electrons (measured in $\mu C/cm^2$ for areas) is needed to fully expose the resist. For PMMA, this will depend on a number of factors:

- The developer used - More powerful developers will remove larger fragments, leading to a lower required dose.
- Acceleration voltage - higher acceleration voltage leads to more energetic electrons. High energy electrons have a lower chance of interacting with the resist, which increases the total dose needed to depolymerize enough chains.
- Resist thickness - a thicker resist will require a higher dose, as more chains will need to be broken.
- Molecular weight of the resist - shorter chains are more sensitive and thus require a lower dose compared to high molecular weight PMMA, e.g. 950k.

To determine the optimal dose for a given set of substrate and resist, a standard method is to utilize a dose matrix. The same set of identical patterns, modeled after the desired final result, is exposed using a range of doses, both lower and higher than the expected dose. The sample is then developed and inspected to determine the optimal dose for the pattern size.

3.2.2 Raith e-LiNE System

The Raith e-LiNE is a scanning electron microscope with extra equipment to enable EBL. The system is shown in figure 3.1, with a schematic diagram in

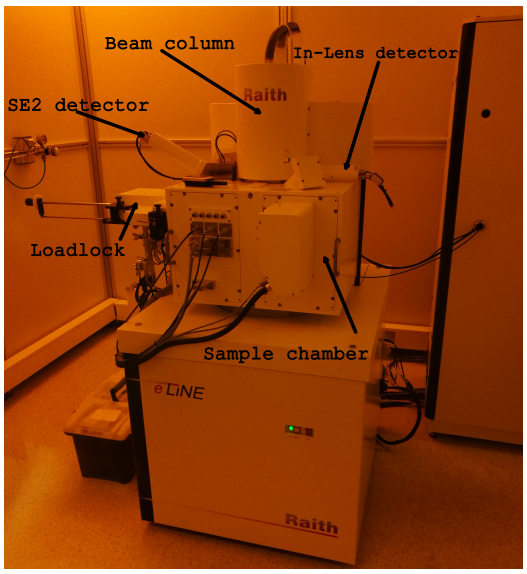

Figure 3.1: Raith e-LiNE system, a combined SEM and EBL tool. A diagram showing the system can be seen in figure 4.1

figure 4.1. EBL is made possible by adding an electrostatic deflector beam blanker, a laser interferometer stage controller and a Faraday cup. These allow rapid switching of the beam, precise positioning of the sample stage and accurate beam current measurements, respectively. All of these elements are integral in implementing EBL. As the beam is scanned across the surface to expose the resist, the exposure time for pixel to be exposed is given by

$$\text{Area dose } [\mu\text{C/cm}^2] = 10^6 \times \frac{\text{Dwell time [ms]} \times \text{Beam current [nA]}}{\text{Step size}^2\ [\text{cm}^2]} \quad (3.1)$$

Usually the current, step size and dose are set values chosen for the sample to be patterned and used to calculate the dwell time. The beam current is dependent on acceleration voltage, aperture and whether high current mode is used. Required dose is determined by acceleration voltage of the system and resist thickness. For high acceleration voltages, the high energy electrons will have a lower probability to interact with the resist, hence a higher dose is needed than for a e.g. 5 kV beam where virtually all electrons are absorbed.

The step size will influence the beam speed, the dwell time and total write time of the pattern. For each pixel patterned, the system will let the beam settle after moving it before patterning the subsequent pixel. For large patterns with a small step size, this may be a substantial part of the total patterning time, up to 50% if a high beam current is used. Small step sizes

with high beam current will lead to high beam speeds as the beam must be scanned faster across the sample. The maximum recommended beam speed for this system is 10 mm/s, but 28.2 mm/s has been used at the system without noticeable artifacts[29].

Larger patterns are split into several write-fields
(100×100 µm for this thesis), where each write-field will be patterned by deflecting the beam in the desired pattern. Between each write-field, the sample stage is moved, which can result in stitching errors between write-fields. This is minimized using the laser interferometer stage controller, which has a resolution of 2 nm[9].

3.3 Electron Beam Evaporator

Electron beam evaporation, also known as electron beam physical vapor deposition, is a technique to coat thin films of a range of materials on samples by heating a source material to vaporization with an electron beam. The system used at the NanoStructures laboratory is a Temescal FC-2000. This system consists of a main vacuum chamber and a smaller chamber on top for loading samples without having to pump the entire chamber. Deposition material is placed in the bottom, in line of sight to the samples to be coated on top, although blocked by two blankers. Currently six materials are available for deposition: gold, glass, chromium, titanium, aluminium and nickel. These materials are situated in individual crucibles of suitable materials. The electron beam is created by applying a 10 kV voltage across a filament to emit electrons perpendicularly away from the deposition material. A powerful magnetic field is set up perpendicular to this direction to accelerate the electrons in a circular orbit towards the material. When the electrons hit the material, they will transfer their kinetic energy into thermal energy, which will heat up the material. The low pressure inside the vacuum chamber means the temperature needed to evaporate the metal is lower than under normal atmospheric pressure.

The magnetic field can be adjusted to move the beam to heat samples evenly, which is particularly important in the case of materials with low thermal conductivity. Glass (SiO_2) has a thermal conductivity lower than 10 % of the other materials. Unless the beam is moved, the heat will not spread and only the middle of the crucible will be evaporated, leading to the formation of a funnel and eventual evaporation of the copper crucible underneath the SiO_2.

Deposition rate is monitored by a measuring the resonance frequency of a quartz microbalance crystal. Change in resonance frequency is given by

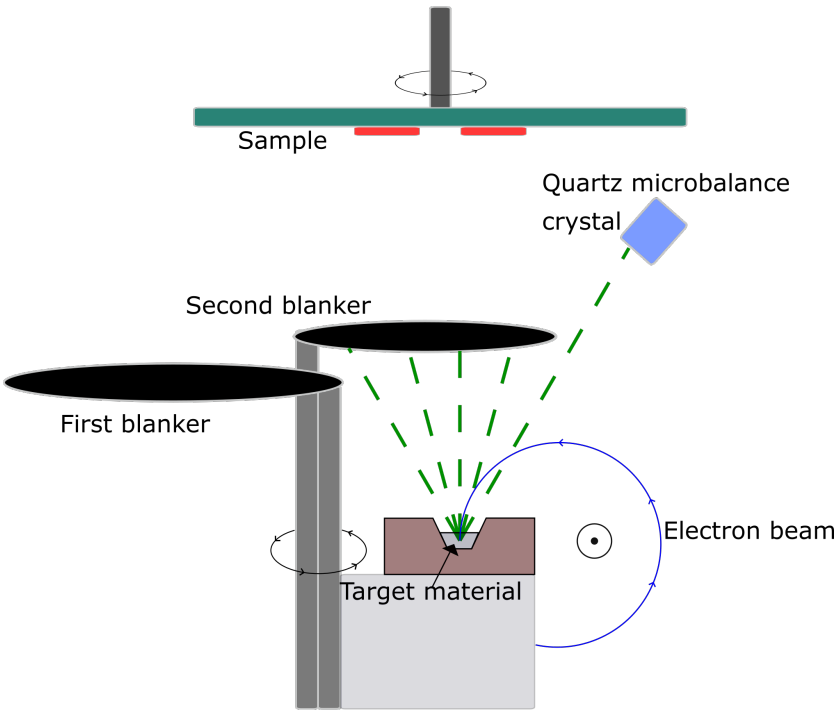

Figure 3.2: Schematic of Temescal FC-2000 system for electron beam evaporation. This is all situated within a vacuum chamber, operating in the 10^{-7}-10^{-6} Torr range.

the Sauerbrey equation[30]:

$$\Delta f = -\frac{2f_0^2}{A\sqrt{\rho_q \mu_q}}\Delta m \tag{3.2}$$

where Δf is the change in frequency, f_0 is the resonance frequency of the unloaded crystal, A is the area of the crystal, ρ_q is the density of quartz, μ_q is the shear modulus of quartz and Δm is the change in mass due to deposition.

One can observe that as material is deposited on the crystal, the decrease in resonance frequency is proportional to mass added. As the density of the material deposited is known, the thickness of the layer can be calculated from

$$\Delta t = \frac{\Delta m}{\rho_d A} = -\frac{\sqrt{\rho_q \mu_q}}{2f_0^2 \rho_d}\Delta f \tag{3.3}$$

after inserting Δm from (3.2). This enables the system to monitor the thickness of deposited layers to 1 nm accuracy and accurate rate control.

An important part of this rate control is the system's two blankers: one

covering the sample and one covering both the sample and the detector. The deposition material is first preheated with both blankers engaged before the crystal is exposed to the vapor, allowing the system to stabilize the rate. The rate is varied using the filament current until it reaches the specified value. At this point, the second blanker opens and the sample is exposed to the vapor. The thickness is continuously monitored until it reaches the specified value and the blankers are engaged to seize the process.

3.4 Reactive Ion Etching

Reactive ion etching(RIE) is a technique used to etch materials without the use of chemical solutions, hence it is also known as dry-etching. While the etchant in chemical etching is a solution, in RIE it is ionized gas, plasma. This technique has the potential of anisotropic etching without the need for special substrate materials, as in the case of single crystal silicon and KOH, see section 3.5.2.

A typical parallel plate reactor RIE-setup consists of two electrodes situated within a vacuum chamber, with the samples placed on the bottom electrode. The top electrode is connected to ground. while the bottom electrode is connected to a power supply through a capacitor blocking DC current flow, but electrically isolated from the rest of the chamber. The power supply is used to create a strong oscillating electromagnetic field between the electrodes, with 13.56 MHz being the most common frequency used[31]. 13.56 MHz falls within the radio frequency regime, hence this is often referred to as a RF-power supply. During operation, gas flows through the chamber.

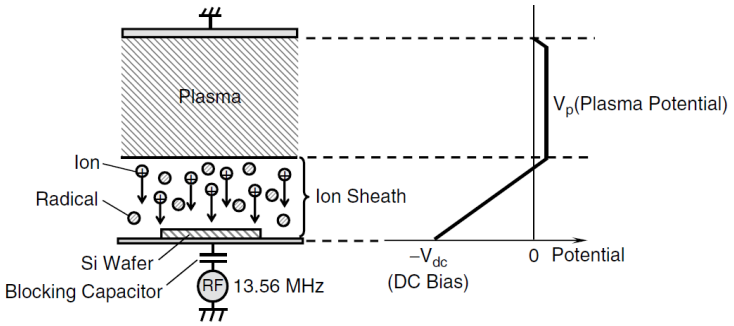

Figure 3.3: Diagram of the chamber used for reactive ion etching showing the electric potential, the plasma and the ion sheath. The plasma contains electrons, ions, radicals and neutral gas molecules. Neutral gas molecules will also be present in the ion sheath. Taken from [32].

The rapidly oscillating electric field is able to accelerate electrons in the gas, but not the heavier ions. This leads to an increased kinetic energy for the accelerated electron and an increased temperature, $> 10^4$ K[32]. A typical RIE-system uses a weakly ionized plasma meaning most of the gas molecules still being neutral, with degree of ionization on the order of 10^{-6}-10^{-4}[32]. The low degree of ionization combined with the low mass of the electrons means the wafer, chamber or gas will not reach the same temperatures.

These accelerated electrons may however be involved in several different processes:

- An elastic collision with a gas atom, transferring kinetic energy.
- An inelastic collision resulting in the ionization of an atom through an expelled electron.
- An inelastic collision causing excitation of an electron from the atom's inner orbitals and the release of a photon after its subsequent decay.
- An inelastic collision where electron capture occurs, leading to negatively charged ion.
- An inelastic collision leading to the dissociation of a gas molecule into more chemically active sub-elements called radicals.
- The electrons hitting the electrodes. Electrons impinging on the top electrode will be carried away to ground, while electrons will accumulate on the bottom electrode, unable to flow due to the capacitor, leading to a negative charge.

The negative charge on the bottom electrode attracts positively charged ions and repels negatively charged ions and additional electrons. This leads to an area near the electrode called the ion sheath, populated by positive ion and radicals, devoid of electrons. The thickness of this sheath is determined by several factors, decreasing with increasing plasma density and decreasing chamber pressure[32].

Mean free path (MFP) of the ions is the average path they travel before colliding with neutral particles in the ion sheath. The ratio between MFP and the thickness is one of the main factors determining anisotropy of the dry-etching. A large ratio indicate few collisions and the ions are able to hit the sample at a normal angle, hence limiting the chemical reaction between the ion and substrate to the bottom of the pattern.

If the reaction is dominated by radicals on the other hand, a more isotropic etching occurs as the radicals are not directed by the electric field. Their movement is decided by brownian motion.

Another factor promoting anisotropic etching is the possibility of tailoring the reaction to create a protective film along **all** exposed surfaces of the sample, protecting it from e.g. etching by radicals. However this protective film will be etched by the ions and/or radicals assisted by ions in the bottom of the pattern, exposing material. This film may be organic polymers, formed from carbon in the gas mixture (e.g. CHF_3) or inorganic films such as SiO_2 formed addition of O_2 during silicon dry-etching.

Ion assisted etching occurs when incoming ions collide with adsorbed radicals on the surface, leading to etch rates several times higher than the observed etch rates from ions or radicals alone[32]. The prevalent theory explaining this is the hot spot model, describing this as an effect of a high local temperature where the ions impinge on the sample[32]. Local elevated temperature will increase the local etch rate from ions and radicals.

The importance of ions in anisotropic etching makes DC-bias essential for determining the etch characteristics. DC-bias will determine the ion energy and hence the local temperature increase. Dry-etching of SiO_2 for instance is a physical-type reaction, meaning it is highly dependent on ion energy rather than exact gas composition[33]. On the other hand, etching of silicon is a chemical-type reaction and its rate will vary greatly with gas composition and pressure[34].

A central characteristic of dry-etching is the actual removal of material from the sample. This requires matching the gas used to the material to be removed. For RIE this means the ion/radicals formed from the gas need to be able to form volatile products to be pumped away. For silicon-based materials, the volatile product is usually SiF_4 with a boiling point of about $-90\,°C$. For aluminium, AlF_3 has a melting point $>1200\,°C$(where it sublimes)[35]. This means aluminium are not easily etched using fluorine-based chemistries, but silicon containing compounds as silicon nitride, silicon dioxide and silicon itself are easily etched by these gases, as long as the energy is high enough to dissociate the compounds. Aluminium is usually dry-etched using chlorine-based chemistries, creating $AlCl_3$.

This all means dry-etching process is dependent on a number of factors, including gas mixture, electrode size, RF-power and chamber pressure, all interconnected. This is a major factor complicating the adaptation of a process from one system to another.

3.5 Chemical etching

3.5.1 Aluminium Wet-Etching

Aluminium etching was performed for the first time at the UiB NanoStructures laboratory as part of this thesis. Aluminium metal is highly reactive and one of the easiest metals to oxidize, having a standard electrode potential of $-1.662\,\mathrm{V}$[36]. However, aluminium will form a stable oxidation layer on the surface, passivating the metal from further oxidation and making aluminium behave as a passive metal. The main passivation layer is an amorphous $\sim 4\,\mathrm{nm}$ Al_2O_3 layer formed within $<1\,\mathrm{ms}$ of being exposed to oxygen[37]. Hence any aluminium etchant needs to be able to break down the Al_2O_3 layer before removing the underlying metal. The contents of the aluminium etchant used in this thesis(Transene Aluminium Etchant Type A) and their roles are:

- 80 wt.% Phosphoric acid (H_3PO_4): Dissolves the Al_2O_3 layer and exposes the bare metal underneath. This is the rate limiting step due to a high activation energy[38].
- 10 wt.% Distilled water(H_2O): Dilutes the etchant to control etch rate.
- 5 wt.% Nitric acid (HNO_3): Oxidizes the Al metal to Al_2O_3, enabling removal by H_3PO_4.
- 5 wt.% Acetic acid (CH_3COOH): Improves wetting of sample and acts as a pH buffer.

H_3PO_4-HNO_3 based etchants are isotropic, meaning the etch rate is the same in all directions. This presents difficulties with masking layer, especially with deep etching, see section 6.2.1.

3.5.2 Silicon Wet-Etching

Chemical etching of silicon in a quantitative manner was performed for the first time at the UiB NanoStructures laboratory as part of this thesis work. Monocrystallinity gives silicon highly anisotropic etch characteristics depending on crystal orientation. For etching in potassium hydroxide(KOH) etch rates in the (100), (110) and (111) crystal planes are approximately 100:200:1, the exact ratios being dependant on etchant concentration, additives and temperature[39]. The wafers used are cut along the (100) plane, usually denoted as Si(100). The (111) plane runs at an angle of

$\arctan\sqrt{2} = 54.74°$ compared to the (100) plane. A square opening in the etch mask oriented along the (110) planes will self limit the etching and form a pyramid with the sides being exposed (111) planes.

The exact mechanism for the large difference in etch rate between (100) and (111) is still being debated, although the etch rate and the bonds involved have been studied and characterized to great detail[40][41].

As the etch rate is highly dependent on crystallographic planes, KOH can be used to manufacture smooth, level surfaces from a silicon wafer. The silicon wafers used has a 200 nm silicon nitride coating on each side. This works as a near perfect mask in KOH, with an etch rate of <1 nm/hr[42]. The etch rate of the (100) plane is on the order of 1 µm/min, enabling highly controllable etch depth. The smoothest (100) surface is obtained with a KOH concentration of 33wt.%, with a roughness value of 0.12 µm[43].

Chapter 4

Characterization Techniques

The following chapter presents the techniques used to characterize the samples throughout the thesis. First the chapter presents the scanning electron microscope and how this is used to create images. Finally the setup used to measure the optical properties of the zone plates is presented. This was set up specifically for this thesis.

4.1 Scanning Electron Microscopy

Scanning electron microscopy (SEM) has been used extensively throughout this thesis to characterize results and inspect samples between processes. This is due to its high resolution and large depth of field, along with convenience of the available system being a combined SEM and lithography system. For more information about the lithography part of the system, see section 3.2.2. A scanning electron microscope works by scanning a highly focused beam of electrons over a sample and measuring the interaction at each point. By doing this over an area, an image can be formed, with each measurement corresponding to a pixel.

A typical SEM-system consists of a column to create the electron beam on top and a sample chamber at the bottom. The entire system is under vacuum to ensure a large mean free path for the electrons. If the system was not under vacuum, the electrons would collide with the gas molecules and scatter. The electrons are usually generated by a field emission gun. This works by applying a high voltage between the tip of a filament and an anode. The strong electric field will draw electrons from the tip, towards the anode. The electron energy is decided by the voltage between these two, also called the acceleration voltage. Acceleration voltage is typically

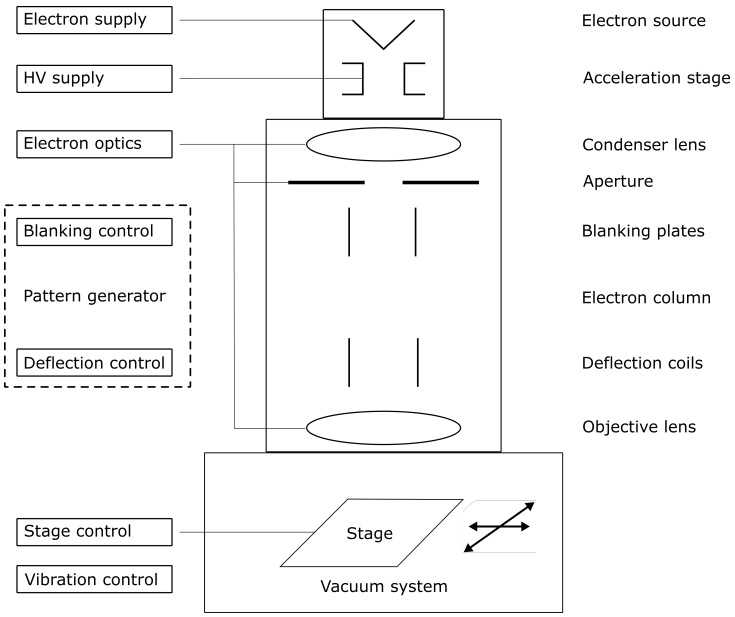

Figure 4.1: Schematic diagram showing the combined SEM and EBL system. Redrawn and adapted from [25]

0.5-30 kV[44]. Several sets of magnetic lenses are used to focus the beam. These consists of conducting coils. By passing current through the coils a magnetic field is created, which will generate a force on the electrons. The current through the coils can be varied to focus the beam. The beam is first focused by a condenser lens before being passed through an adjustable collimating aperture to limit the amount of electrons and shape the beam. Before hitting the sample, the beam is focused by additional lenses and pass through deflection coils. The deflection coils are used to move the beam within the xy-plane and facilitate scanning across the sample.

The image signal originates from detection of secondary electrons, created by ionization of the sample[45]. The system used in this thesis is equipped with two detectors, an InLens detector and a secondary electron (SE2) detector. The InLens detector is situated in the column, meaning it will only detect secondary electrons created in the sample volume. Its position directly above the sample creates an even image without shadowing.

The SE2 detector is an Everhart-Thornley detector situated at an angle to the sample. This attracts electrons by applying a positive bias of $\sim$200 V to the detector. Due to the angle compared to the sample, this detector will give extra topographical information and shadowing. This detector will also detect SE3, secondary electrons generated by backscattered electrons hitting chamber walls.

4.2 Optical Testing of Zone Plates

Motivated by a desire to characterize the performance of the zone plates, an experimental setup using a laser was constructed. The setup was inspired by a similar setup previously used within the group to test a Beynon Gabor zone plate[46].

A laser source (Thorlabs TLS001-635) was used to provide a divergent beam which was passed through a variable polarization filter. The purpose of this filter is to vary the beam intensity. A lens (Thorlabs AC254-150-A-ML) was placed 150 mm downstream from the source, putting the source in the lens' focal spot. This creates a parallel beam to illuminate the sample, set approximately 300 mm away from the lens, mounted on a rail along with the detector (Thorlabs DCC1545M). The detector was free to move along optical rail, allowing adjustments to ensure positioning of the detector at the zone plate's focal length. A 30 mm lens tube was mounted on the detector to reduce noise. Pixel size of the detector is 5.2 µm. The setup utilizes a

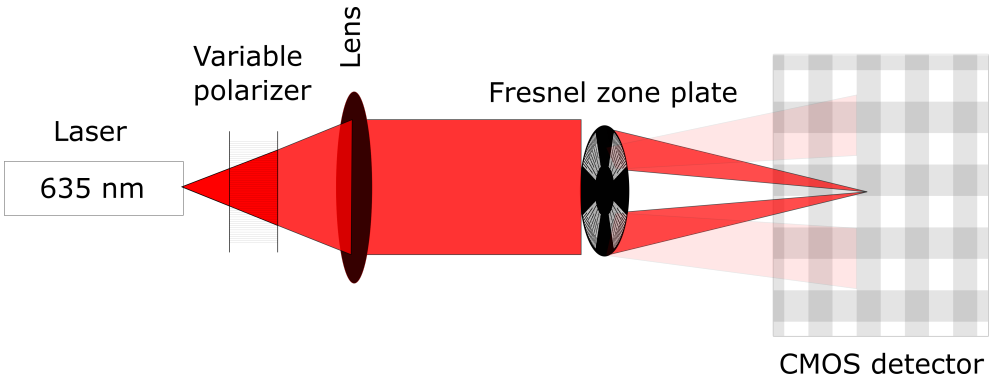

Figure 4.2: Schematic showing the optical setup for testing zone plates. The lens is situated 150 mm from the laser source to achieve a parallel beam. Using a 635 nm laser source yields a first order focal length of 9.45 cm for the zone plates.

635 nm point source laser. This is comparable to the 100 nm wavelength BEC intended to use with the zone plates. However, the change in wavelength will alter some of the optical properties. The focal length and hence the depth of field of the zone plates are changed. The zone plates are fabricated to achieve a focal length of 60 cm with a 100 nm source wavelength. As the focal length of a given pattern is inversely proportional to the wavelength, see (2.5), the expected focal length using 635 nm is $\frac{60\,\text{cm}}{6.35} = 9.45\,\text{cm}$

A power meter was used to measure the optical power output of the laser source at different input powers in order to enable comparison between

measurements taken at varying input power.

Chapter 5

Methods

This chapter presents the experimental processes used to pattern aluminium, SiO_2, chromium, silicon and silicon nitride. The ideas and intentions behind the different processes is discussed. The silicon section contains the background for the different patterns and how they assist in realizing the intended final result. Finally the experimental procedure needed to replicate the results is described.

Zone plates for focusing matter waves have previously been fabricated within the group[7][9]. These zone plates were however fabricated for $\lambda_{dB} = 0.055$nm and had a maximum diameter of 400 µm. This diameter would not cover the the first zone of the pattern created with the parameters in table 2.1, which has a diameter of 612 µm. Additionally, previous work patterned a free-standing silicon nitride membrane. This is not possible for a zone plate covering a 5×5 mm area required for this thesis as the thin nitride can not support itself over these distances after patterning.

5.1 Pattern Creation

The pattern for EBL was created by modifying the zone plate pattern from a Raith software. This software uses the desired object distance, focal length and diameter to create a list of circles with widths satisfying (2.5). Throughout this thesis, the zone plates were created for a 100 nm wavelength incident plane wave with a focal length of 60 cm. A typical example of an element in the zone plate pattern file is shown in figure 5.1.

A custom python script was written to create support bars, to remove unwanted parts of the pattern and to alter the pattern. This is achieved by

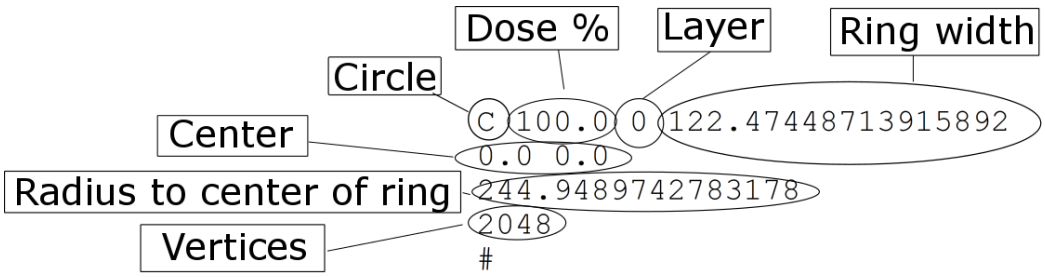

Figure 5.1: Typical ASCII code defining a single ring segment in a zone plate EBL pattern

creating a pattern of the unwanted areas in a layer separate from the original zone plate and using the e-LiNe software's built in Boolean subtract function to remove these parts from the pattern. The complete python script can be found in the appendix.

A central stop is created by going through the radii of each zone until a zone larger than the central stop size is found. The inner radius this zone is then used to create an ASCII element similar to figure 5.1.

Main support bars consists of rectangles connecting the central stop to the wafer along diameters every $\frac{360^\circ}{16} = 22.5^\circ$. The points of the rectangle are rotated around the center by using the transformation:

$$\begin{bmatrix} x' \\ y' \end{bmatrix} = \begin{bmatrix} cos\theta & -sin\theta \\ sin\theta & cos\theta \end{bmatrix} \begin{bmatrix} x \\ y \end{bmatrix} \tag{5.1}$$

where x' and y' is the new coordinates after rotation and θ is the rotation in radians, The coordinate system is centered at the middle of the zone plate.

Secondary support bars are created when $\frac{length}{width}$ of the freestanding element is less than some factor. Previous work has used a factor of 30 for silicon nitride zone plates with diameter $< 400\,\mu m$[9]. However, for the 5 mm zone plates in this thesis, a factor of 14 was required for structural integrity, see section 6.6. This factor is calculated for every zone radially and the inner radius of the zone is set as starting point for a new support bar whenever it is exceeded. The support bars are distributed using (5.1), bisecting the previous set. Four circular sectors are created using ASCII arc elements to remove or keep the diagonals of the pattern.

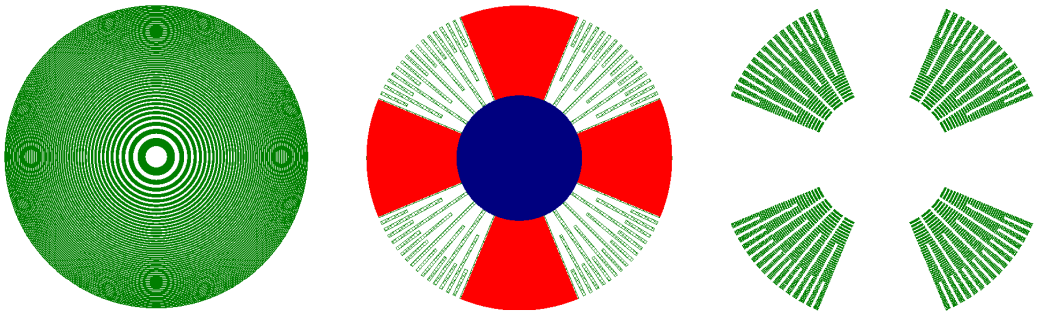

(a) Original zone plate pattern

(b) Parts to be removed, created with python script

(c) Finished pattern after removing (b) from (a)

Figure 5.2: Pattern creation by creating structural support and blocking elements and their subsequent removal from the zone plate pattern.

5.2 Aluminium Zone Plate

5.2.1 Material Choices

The first objective was to find a suitable material that could be patterned using the chemicals or instruments available at the facilities. Chemical etching, wet etch, was initially chosen as the desired technique for patterning the sample, due to the expected size of the structures. Available etchants included nickel, aluminium, titanium, tungsten and chromium along with common acids and bases. Possible masking materials from the electron beam evaporator was titanium, gold, SiO_2, aluminium, nickel and chromium. The compatibility between substrate etchants and mask materials is shown in table 5.1.

		Masking materials					
		Ti	Au	SiO_2	Al	Ni	Cr
Etchants for substrate	Nickel TFB	✓	✓	✓	✕	✕	✕
	Aluminium Type A	✓	✓	✓	✕	✕	✕
	Titanium TFT	✕	✓	✕	✕	✓	✓
	Tungsten TFW	✓	✓	✕	✕	✓	✕
	Chromium 1020	✓	✓	✕	✕	✕	✕
	Hydrofluoric acid (HF)	✕	✓	✕	✕	✓	✓

All etchants distributed by Transene Company, Inc.
✓-compatible ✕-etches

Table 5.1: Masking material and etchant compability.

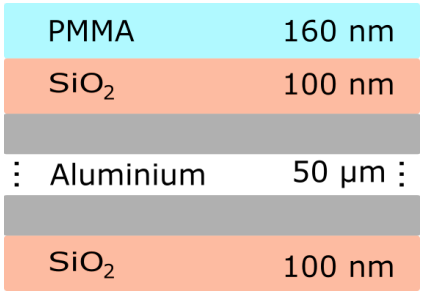

Figure 5.3: Cross section of the stack used for patterning aluminium

Although gold looks like a promising masking material because of high chemical stability, it would be problematic to transfer the pattern from PMMA to the gold masking layer. Common available chemical etches for gold will attack the PMMA and while there are more specialized etches for microfabrication this was not further looked into. Gold also has problems with adhesion between the metal and resist due to the lack of oxide layer[47]. Dry etching of gold is mainly chlorine-based[47], which is not available at the system used. Dry etching of gold with CF_4 and Ar is however possible[48]. This method has problems with re-deposition of gold on the surface caused by the low volatility of AuF_x, which would interfere with other parts of the pattern. The actual material removal is believed to be based on sputtering of the AuF_x by-product layer by Ar[47].

Al-SiO_2 was eventually chosen as the substrate-masking pair due to four main reasons:

- The aluminium etchant is specifically developed to not attack SiO_2.
- Etch rates suitable for the amount of material to be removed
- Etch resolution down to 1 µm lines, according to manufacturer.
- Aluminium's high strength to weight ratio.

15 mm diameter hard tempered aluminium discs were supplied by Goodfellow. Thickness was chosen to be 50 µm in order to achieve a compromise between strength and ability to be processed. The specified purity was 99.0%. Before being put into use, the samples were thoroughly cleaned in an ultrasonic baths of acetone, methanol and IPA for 20 minutes each followed by N_2 drying to remove any residue leftover from the fabrication process.

5.2.2 Sample Holders

Sample holders had to be built in order to ensure a level surface for the aluminium discs and the blueprints were drafted using Autodesk Inventor. The holder consists of two rings to fixate the Al discs in between, enabled by threaded holes in the bottom ring. The technical drawings can be seen in figure 5.4 and 5.5. Both parts has a large central hole, allowing access to the substrate from both sides.

As the goal was to integrate these holders into the entire process, they would have to be compatible with the Al etchant. PEEK (Polyether ether ketone), a chemically resistant polymer, was initially chosen as material for the holders. PEEK is compatible with H_3PO_4, HNO_3 (at this concentration), acetic acid and the solvents used for cleaning. 316L stainless steel were later used as material for a second set of holders. 316L steel is resistant to all chemicals used except for high temperature H_3PO_4, but the corrosion is negligible at the temperatures and duration used. The addition of HNO_3 also decrease the corrosion of 316L steel in phosphoric acid[49]. The fabrication of the sample holders were performed by the in-house mechanical workshop at UiB. To avoid any contamination from lubricants used in the fabrication process the parts were ultrasonically cleaned for 20 minutes in acetone, methanol and isopropyl alcohol.

5.2.3 Pattern Transfer

From PMMA to SiO_2

Reactive ion ethcing were used to transfer the PMMA pattern made by EBL. The recipe used were based on [50], which had to be adapted to the Plasmatherm 790+ system available, see section 6.1. This recipe improves the selectivity between PMMA and SiO_2 by splitting a long CHF_3 and Ar dry-etch into several smaller etches, interrupted by N_2 flushing. The SiO_2 etch rate remains the same, but the PMMA etch rate is halved. This is because the continuous process has temperatures up to 150 °C, close to PMMA's melting point of 160 °C, with the main contribution being radiative heating[51]. This means cooling of the electrode is not effective in alleviating the problem. The temperature rises during the first minutes of etching and stabilizes[52]. By breaking the process up and letting the sample cool down between each step, the PMMA etch rate is minimized and the selectivity between PMMA and SiO_2 is improved. This process was used to etch both 30 nm and 100 nm thick layers of SiO_2 using a 160 nm PMMA layer, see section 6.1.

Dry-etching of SiO_2 is mainly ion-based[53]. This fact, coupled with the

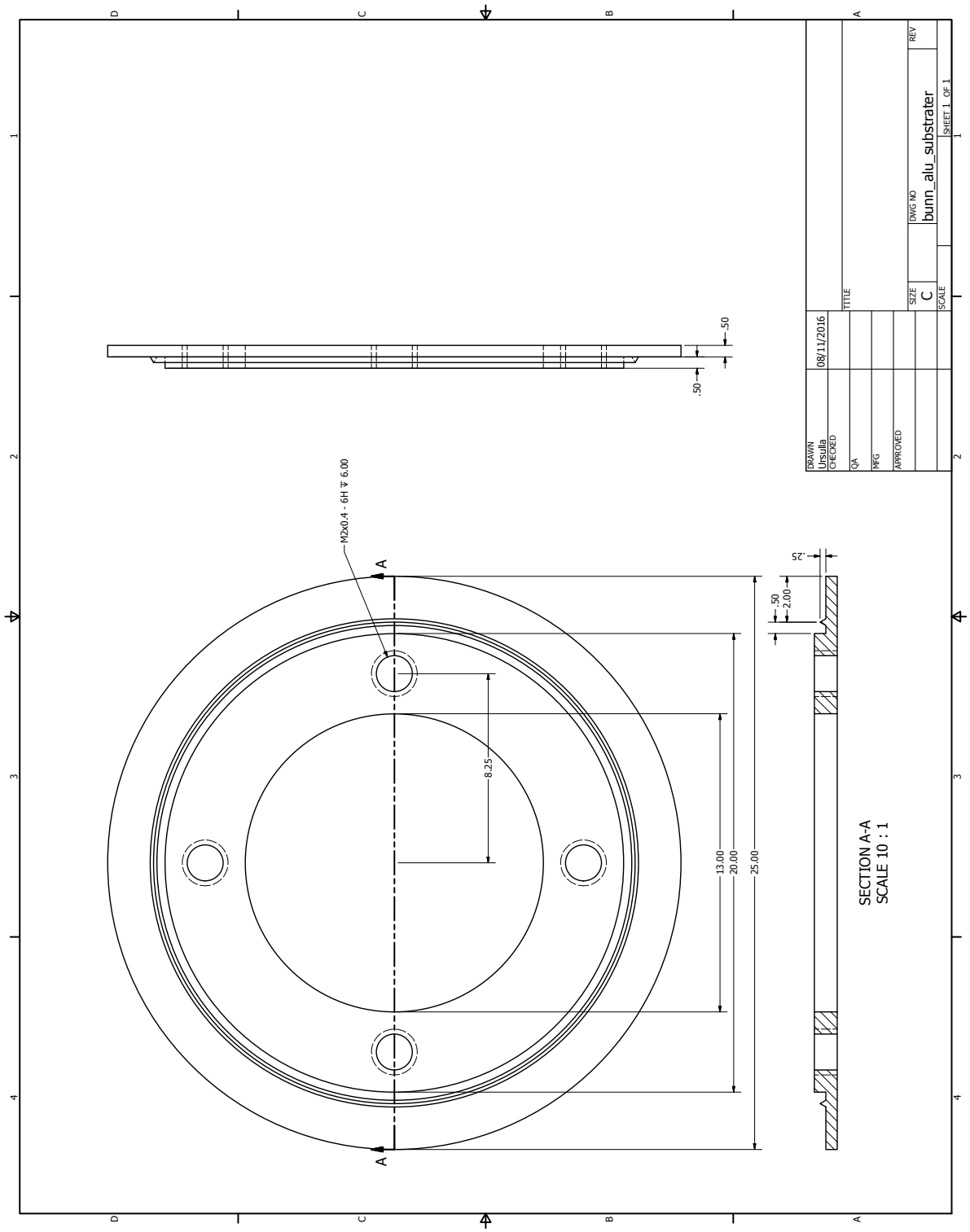

Figure 5.4: The bottom part of the sample holder

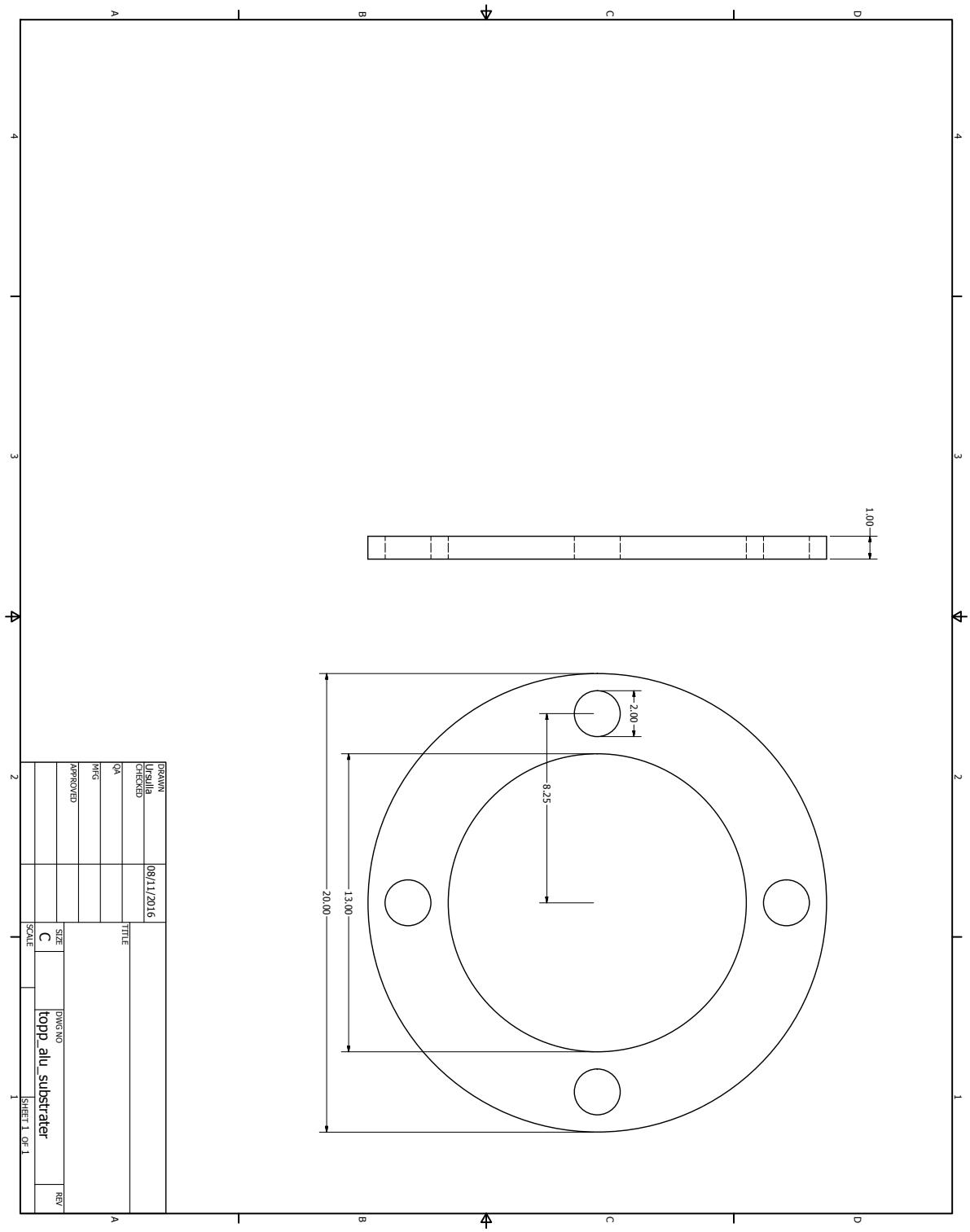

Figure 5.5: The top part of the sample holder

high activation energy of the SiO_2 reaction places high weight on the importance of DC-bias in SiO_2 dry-etching. The recipe had to be adapted by varying process variables to obtain the same bias as reported by Wuest et al. (500 V)[50]. DC-bias is proportional to RF power due to a higher amplitude of the electrical field, attracting more negative electrons to the negative electrode. This leads to a higher potential difference between the two electrodes, a higher DC-bias. DC-bias can also be controlled by varying the chamber pressure, generally showing an inverse proportional dependence. Lower pressures increase the mean free path of ions in the chamber. This increases the transport of charged particles to the surface, thereby increasing the bias. Pressure changes has different effects on processes depending on the etch-mode (ionic, radical, sputtering) and as our gas mixture has the possibility to include all three reactions, changing the pressure was abandoned as method. This left the variation of RF power as the only real alternative to find a correct bias.

From PMMA to Silicon Nitride

The same principle used in adapting the SiO_2 recipe was used to adapt a recipe for pattern transfer into silicon nitride. The chemistries involved is similar, hence bias is an important factor in this process as well. For results from this process, see section 6.4.

5.3 Silicon Substrate Zone Plates

Monocrystalline silicon is a widely used material for Microelectroechanial systems (MEMS), photovoltaic applications and integrated circuits. The advantage of this wide use is well developed processes for microfabrication of silicon, which can be taken advantage of. Monocrystalline means the material consists of only one crystal orientation, spanning the entire material. In contrast, a polycrystalline material consists of isolated monocrystalline regions that can be anywhere from nanometer sized to several millimeters.

Silicon was chosen as the next material for realizing the patterns needed for the zone plates due to its well-behaved etching characteristics and the availability of a near-perfect etch mask, see section 3.5.2. These etch characteristics enables the fabrication of thin, even membranes, which can subsequently be patterned.

As previously mentioned, silicon wafers with nitride coating have been used at the UiB NanoStructures laboratory to produce Fresnel zone plates before. However, this process used smaller areas, where all of the silicon was

removed, leaving a free-standing membrane of nitride. Nickel was deposited onto the sample to form support bars, and the nitride layer was patterned using EBL followed by several RIE-steps. This process is not possible for the large zone plates in this thesis as the nitride would not be able to support itself across the 5×5 mm area after being patterned.. Time was also a factor: to use the previous mentioned process, custom photolithographic masks for the support structures would need to be purchased, which would delay the start up.

5.3.1 Silicon Membrane Fabrication

Silicon membranes was fabricated using single side polished 525±25 µm thick Si(100) wafers, boron p-doped to 1-30 Ωcm from Si-Mat. The wafers are LPCVD (low pressure chemical vapor deposition) coated with 200 nm low-stress silicon nitride on both sides. Low-stress nitride has a higher silicon content than the usual stoichiometric Si_3N_4, which tends to have residual intrinsic stress and are subsequently more prone to breakage[54]. As previ-

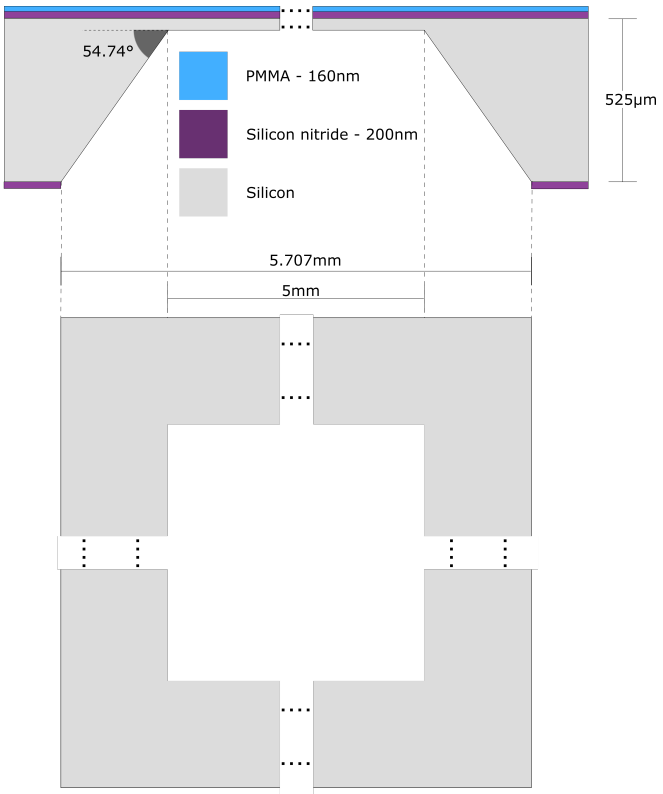

Figure 5.6: Diagram showing cross section and back of silicon membranes.

ously mentioned the angle between (100) and (111) is 54.74°, which means to realize a 5x5 mm membrane after etching 500 µm, the mask must have a total width of at least

$$5\,\text{mm} + 2 \times \left(\frac{500\,\mu\text{m}}{\tan 54.74^\circ} \right) = 5.707\,\text{mm}$$

Quadratic improvised photomasks were milled from PVC by the in-house mechanical workshop. Using photolithography and RIE, a quadratic opening in the nitride layer was created, exposing the underlying silicon wafer. For process specific details see section 5.4. A diagram showing the membranes can be seen in figure 5.6. Typical thickness of the membrane was 40 µm The angle between the (111) planes and (100) could also be used to monitor the etch depth using the SEM. By measuring the horizontal width of the (111) plane, the depth was calculated using

$$d = w \tan 54.74^\circ = w\sqrt{2} \tag{5.2}$$

where d is the measured depth and w is the measured horizontal distance from the top to the bottom of the (111) plane. Secondary depth measurements were also performed by precisely measuring the working distance in the SEM at several points along the membrane surface. By calculating the difference in working distance from the top of the frame to the bottom of the membrane, precise depth measurements could be obtained. Focusing was done by the residue left on the silicon surface, which was in the 100 nm range. The residue is due to oxides from trace metals in the KOH pellets which will precipitate when the sample is removed from the KOH solution[55].

Etchant Consumption

To calculate the amount of KOH consumed by etching and subsequently investigate the reusability of the KOH solution one needs to consider the chemical reaction

$$\text{Si} + 2\,\text{OH}^- + 2\,\text{H}_2\text{O} \longrightarrow \text{Si(OH)}_4 + \text{H}_2$$

which means we consume 2 mole KOH per mole of Si. The total volume etched per wafer is approximately

$$V_{etched} = (5\,\text{mm})^2 \times 500\,\mu\text{m} = 1.25 \times 10^{-8}\,\text{m}^3$$

Using $\rho_{Si} = 2329\,\mathrm{kg/m^3}$, the total mass for each wafer is

$$m_{etched} = 2329\,\mathrm{kg/m^3} \times 1.25 \times 10^{-8} m^3 = 29.11\,\mathrm{mg}$$

Molar mass of silicon is 28.05 g/mol giving $n_{etched} = 1.04\,\mathrm{mmol}$.
As the solution was prepared using 151 gKOH = 2.69 mol. Each wafer then consumes

$$\frac{2 \times 1.04\,\mathrm{mmol}}{2.69\,\mathrm{mol}} = 0.08\%$$

of the etchant. To change the concentration of the solution by 1wt.% one would need to consume 3% of the KOH, or 37.5 wafers. It is safe to assume this will not influence the etch rate significantly.

5.3.2 Silicon Zone Plate

The idea behind the silicon zone plate was to use the membranes manufactured in section 5.3.1 and pattern the nitride layer using PMMA. The nitride layer would subsequently serve as a mask for KOH etching. Because the (111) etch rate is 1% of the (100) rate, any rectangular pattern oriented along (110) would not expand while etching the zone plate into the membrane. However, this means that in order to achieve a specified opening at the bottom of an open zone, the open zones in the EBL pattern has to be expanded. Every open zone would have sides consisting of (111) planes, a similar situation to the method used to measure etch depth in the membrane fabrication. Every zone in a pattern would need to be adjusted according to

$$w_{new} = w_{old} + 2\left(\frac{t}{\tan 54.74^\circ}\right) = w_{old} + t\sqrt{2} \tag{5.3}$$

where w is the width of the open zone patterned and t is the **desired final** thickness of the membrane. This was done using the previously mentioned python script, see Appendix. This also meant that membrane thickness control were of paramount importance to achieving correct zone widths and puts constraints on the final thickness of the membrane. Using a thick membrane would eventually lead to overlap of the outer zones in the EBL pattern. To illustrate the progression of etching a rectangular opening in the masking layer, a rough simulation was performed using ACES[56]. The rectangle is oriented at 45° to (110). This would pose a problem when fabricating the silicon zone plate. The open zones will overlap, depending on the angular deviation from the (110) plane. The elements positioned on the diagonals

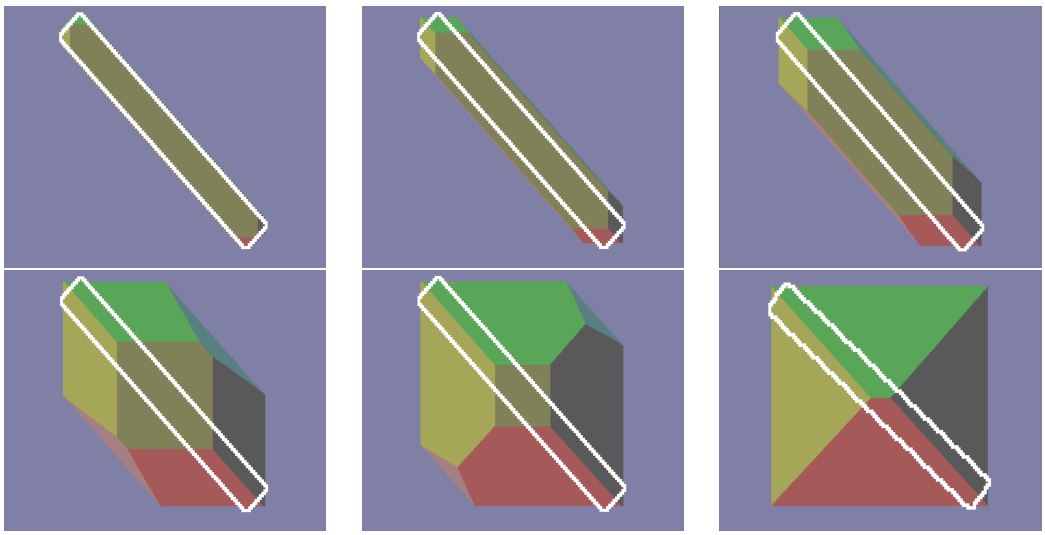

Figure 5.7: Simulation illustrating how a line progresses in KOH etch. The white line is the initial mask opening and the different colors represent different crystal planes. This simulation was performed using the free software ACES[56].

from the center would be most affected. As an attempt to minimize this effect, the pattern was removed in the angular intervals $[\frac{\pi}{8}, \frac{3\pi}{8}]$, $[\frac{5\pi}{8}, \frac{7\pi}{8}]$, $[\frac{9\pi}{8}, \frac{11\pi}{8}]$ and $[\frac{13\pi}{8}, \frac{15\pi}{8}]$. This would halve the opening ratio, but is a necessary step towards realizing the desired structures.

5.3.3 Silicon Nitride Zone Plate

The author was surprised by the resilience of the silicon nitride layer. During the attempted fabrication of silicon zone plates, it was discovered that the nitride tolerated suspension over gaps in the 100 µm range, which can be seen in figure 6.14-6.19. This prompted the idea to fabricate a free-standing zone plate with the nitride acting as the diffraction surface and the silicon forming the support bars. For this application, the nitride elements would also be wider, as the thickness correction would not be necessary.

However, this called for a reliable method of removing the silicon underneath the open zones without removing the silicon on the support bars or damaging the nitride layer. This was eventually solved by using the problems faced creating the silicon zone plates as a tool. By rotating the blocked zones 45° compared to the pattern used in section 5.3.2, one can maximize the open zones' angular deviation from the (110) plane. This leads to complete overlap

of all open zones, and their subsequent etching.

In theory, this overlap should not destroy the support bars, as the pattern will not extend in that direction, see figure 5.7 and imagine each of the short ends to be connected to a support bar.

5.3.4 Chromium Zone Plate

As an analogue to the free-standing zone plates chromium zone plates was fabricated on glass substrates. The intended purpose of this was to verify the effectiveness of the pattern and investigate the role of support bars and blocked segments on the resulting performance using an optical setup. For more information about this setup, the results and the fabrication see section 4.2, 6.3 and 5.4.6, respectively.

5.4 Experimental Procedure

5.4.1 Resists

PMMA

The PMMA used throughout the thesis is 950K AR-P 672.08 (Allresist GmbH) diluted 1:1 with anisole. Before coating, the samples were fixated on a silicon wafer designated for spin coating. This wafer has Gel-Pak adhesive pads to ensure stiction to the samples being coated. A vacuum pump holds the wafer in place on the spin-coater (Chemat KW-4A).

Using a pipette, the PMMA was placed drop-wise on the sample until it was covered. For all samples the settings was 500RPM for 9 seconds followed by 4000RPM for 60 seconds. Immediately after finishing spin coat the samples were baked on a 175 °C hotplate for 5 minutes to evaporate the anisole and bake the resist.

AR 600-56 (Allresist GmbH) was used to develop the PMMA patterns. The samples were immersed in the developer for 90 seconds before the developing was stopped by rinsing with isopropyl alcohol for 20 seconds and the samples were blown dry with N_2.

Photoresist

Using the same setup as for PMMA, AR-P 3540 (Allresist GmbH) photoresist was spin coated onto both sides of silicon wafers. Settings for photoresist

coating was 600RPM for 18 seconds and 4000 RPM for 60 seconds followed by a 100 °C bake for 1 minute.

Photolithography was performed on the rough side using a crude setup with UV-LEDs. The PVC photo mask was manually aligned using the cleavage edges on the wafers as reference. Exposure time was 90 seconds. The developer consisted of 1 part AR 300-35 (Allresist GmbH) and 2 parts DI-water. Development time was 40 seconds and was followed by a thorough rinse in DI-water and N_2 blow drying.

5.4.2 EBL Patterning

Patterning has been done with various settings throughout this thesis, dependant on available time and required resolution. The acceleration voltage has remained unchanged, in order to ensure consistent resist sensitivity, see section 3.2.1. Both 30 µm and 60 µm apertures have been used, both with and without high current mode, depending on sample. High aperture and current amplifies charging issues, hence it may be problematic to use on insulating samples and challenging to achieve sufficient focus. High beam current significantly reduces write times for large patterns, for more equipment specific information about this topic see [29].

Pattern Placement

In order to position the pattern, the back of the wafer was mapped during depth measurements. As long as the wafer was secured to the SEM wafer holder using the same edge, the orientation could be preserved. An origin visible and recognizable from both sides of the sample was chosen, and the angle correction was used to find the rotation of the pattern. Two points along a the interface between a (111) and the (100) plane was used to find the proper angle and the coordinate system was adjusted using this. Subsequently, the positioning of the four corners of the silicon membrane was noted.

When positioning the pattern during EBL, the coordinate system has to be adjusted to match the measured one. First, the origin needs to be located and the angle adjusted to the negative of the previous value. This is because the coordinate system is mirrored across the horizontal line when the wafer is flipped. When the coordinate system is mirrored, the y-values of the corners will be negated compared to the origin. The lower left corner is then used as the final position of the pattern.

5.4.3 Pattern Transfer Reactive Ion Etch

PMMA to SiO_2

This process was investigated using silicon wafers with a 100.7 nm SiO_2 layer deposited by EBPVD. 3 mm long sets of 100, 200 and 300 nm wide lines in PMMA were written using EBL. The initial attempts used identical settings as [50]: 25sccm CHF_3, 25sccm Ar, 30mTorr pressure and 200 W RF power. A total of 6 minute etching was split into 3x2 minute cycles, expecting a etch selectivity SiO_2/PMMA of approximately 2.5.

After the recipe was fully adapted to our system, the process was split into 30 second etches, with 90 second N_2 flushing between each step, with total number of steps varying with SiO_2 thickness. Gas flow for the process was 25sccm Ar and 25sccm CHF_3 at 30 mTorr. RF power was set to maximum, 600 W.

The Plasmatherm 790+ system was not able to uphold the set 30 mTorr N_2 flushing pressure so the flushing step had to be split into processes short enough to not stay under the set flushing pressure for an extended period. This will trigger an alarm and full opening of the throttle valve.

Photoresist to Nitride

To transfer the pattern from the photoresist to the nitride a soft etch followed by a hard etch was utilized. This was adapted from methods used previously at the facilities. The soft etch consisted of 15 sccm CF_4 at 10 mTorr, at 100 W for 17 minutes. The hard etch was 45 sccm CF_4 and 5 sccm O_2 at 40 mTorr with RF power set to 350W, for 3 minutes. The samples were finished of with a 2 minute soft etch to ensure opening of the pattern, which is unproblematic due to a large excess of photoresist left after RIE. Original thickness of photoresist was $\sim$1.4 µm compared to the 200 nm nitride.

PMMA to Nitride

The recipe to RIE silicon nitride from a PMMA mask was adapted using the same methods as for the SiO_2-recipe adaptation. This was carried out on the same wafers used in section 5.3.1. The RF-power was increased until the bias matched value used by Wuest et al.[50] at their system. The gas flow was 50 sccm CHF_3, 5 sccm O_2 with a chamber pressure of 45 mTorr. Total etch time was 14 minutes to ensure a fully opened pattern.

To characterize the process, EBL was used to write 1, 5, 10, 20 and 30 µm wide, 3 mm long, lines in PMMA, using the fast write settings outlined

in section 5.4.2. The wafers were dry-etched for 3 minutes and cleaved to investigate etch rates and uniformity of larger patterns.

5.4.4 Aluminium Wet-Etch

To etch aluminium, ∼50 mL Transene Aluminium Type A etchant was poured in a beaker situated in a 200 mL water bath. To ensure a stable temperature the setup was heated on a hotplate with integrated temperature probe. The temperature was measured in the water bath to avoid etching the metal probe. A glass thermometer was placed in the etchant to monitor the etchant temperature in parallel. The etch rates supplied from the producer is shown in table 5.2

Temperature [°C]	Etch rate [nm/s]
25	3
40	8
50	10
65	24
75	55

Table 5.2: Etch rates for different temperatures with Transene Aluminium etchant Type A

5.4.5 Silicon Wet-Etch

The KOH solution was prepared by dissolving 151 g KOH pellets (Merck Millipore KGaA) in 302 g of DI-water. Dissolving KOH is an exotherm process and the pellets must be added in several steps to avoid high temperatures. Etching was carried out in a closed quartz beaker with a water cooled reflux condenser. Quartz is used to minimize beaker corrosion, while the reflux condenser is used to ensure a stable concentration. As the etching is carried out at 80 °C for several hours, the evaporation of water would be considerable, leading to increasing concentration, uneven results and etch rates. A Stuart CB160 hotplate without temperature control was used to heat the solution. This was set to ∼130 °C throughout this thesis which resulted in a solution temperature of approximately 75 °C, varying with position and depth of etchant. The samples were cleaned with acetone to remove any resist before being placed on custom PTFE(teflon) holders. Initial attempts at membrane fabrication etched the samples standing up to ensure separation

of the wafers and facilitate flow of H_2 gas, while later attempts used a flat holder.

After etching the samples were thoroughly rinsed in DI-water before being lightly sprayed with IPA and blown dry with N_2. IPA spray is used to ease the drying process of the hydrophilic nitride surface.

The samples were etched together until an approximate depth of 460 µm before being finished individually with frequent depth measurements and small etch steps to ensure the correct thickness.

5.4.6 Chromium Zone Plate

The zone plates were fabricated on microscope slides. Before being coated with chromium the slides were cut into suitable sizes and cleaned using the procedure outlined in [29]. The slides were immersed in ultrasonic baths of acetone and isopropyl alcohol for 10 minutes each before being rinsed under de-ionized water for 2 minutes. Between each step the samples were blown dry using N_2. After the water rinse, the samples were baked on a 115 °C hotplate for 5 minutes to ensure a dry surface. 100 nm Cr was deposited on the samples by EBPVD before being spin coated with 160 nm PMMA using the standard settings.

After the patterns were exposed using fast-write settings, see section 5.4.2, and developed, baring the underlying chromium layer. The wafers were submerged in room-temperature Transene 1020 Chromium etchant for approximately 80 seconds. The progress was checked manually with the SEM until the chrome layer was removed. Total etch time was initially estimated by etching a small piece of Cr-coated glass until transparent. Room temperature was chosen over the recommended 40 °C due to ease of use, more controllable etch depth and no noticeable quality difference.

Chapter 6

Results and Discussion

This chapter presents the results achieved in this work together with discussion. First, the process of patterning aluminium is presented. An important part of this process was enabling pattern transfer between PMMA and the SiO_2 mask via dry-etching. SEM pictures showing the dry-etching results and etching of aluminium is included. Subsequently, results from the silicon membrane fabrication is shown and discussed. These membranes served as the sample for the silicon and silicon nitride zone plates. Important results from these two processes are presented via optical and SEM micrographs. Finally the results from optical testing of the nitride and chromium zone plates are presented.

6.1 Reactive Ion Etching SiO_2

Inital attempts of SiO_2 dry-etching used the same settings as Wuest et al., etching for 2.5 minutes without flush steps. Using the etch rates from [50], this was expected to etch 100 nm SiO_2 and 50 nm PMMA. The results can be seen in figure 6.1.

The SiO_2 layer inside the lines remains virtually untouched, suggesting a vastly different etch rate than the expected 40 nm/min. Apparent thickness of the PMMA layers varies greatly between the two samples, suggesting deformation of the edge during cleaving.

To find a suitable RF-power value for the SiO_2 dry etch, the bias was measured at different settings, see figure 6.2. The maximum RF-power for the system is 600 W, resulting in a bias of 476 V, close to the specified value of 500 V.

Using these new settings, a new set of lines were dry-etched with a total etch time of 3 minutes, using the cyclic etching outlined in section 5.2.3 and the correct bias. The results can be seen in figure 6.3.

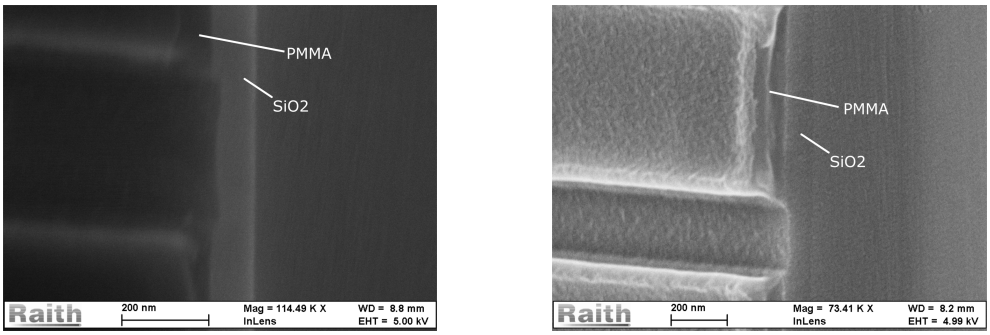

(a) (b)

Figure 6.1: Initial results of dry etching SiO_2 200 nm lines, taken at 45° after cleaving the wafer. (a) shows the uncoated sample, while (b) is sputter coated with AuPd to enhance contrast (18 mA, 15s)
25 sccm Ar, 25 sccm CHF_3, 30 mTorr, 200W, 2.5 minutes.

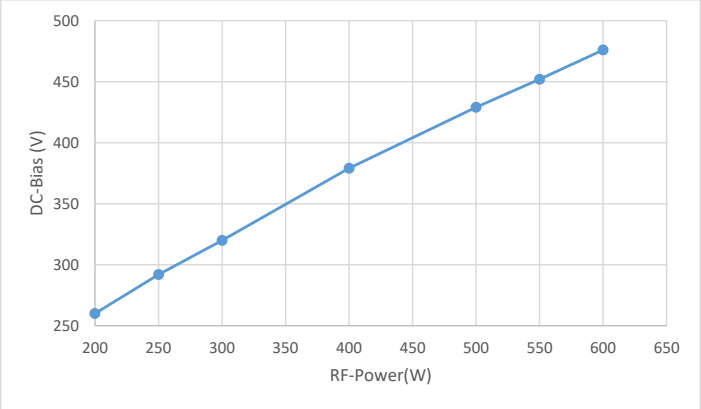

Figure 6.2: Measured DC-bias of Plasmatherm 790+ system for different power settings using 25 sccm Ar, 25 sccm CHF_3, 30 mTorr. Error bars are not visible at this scale.

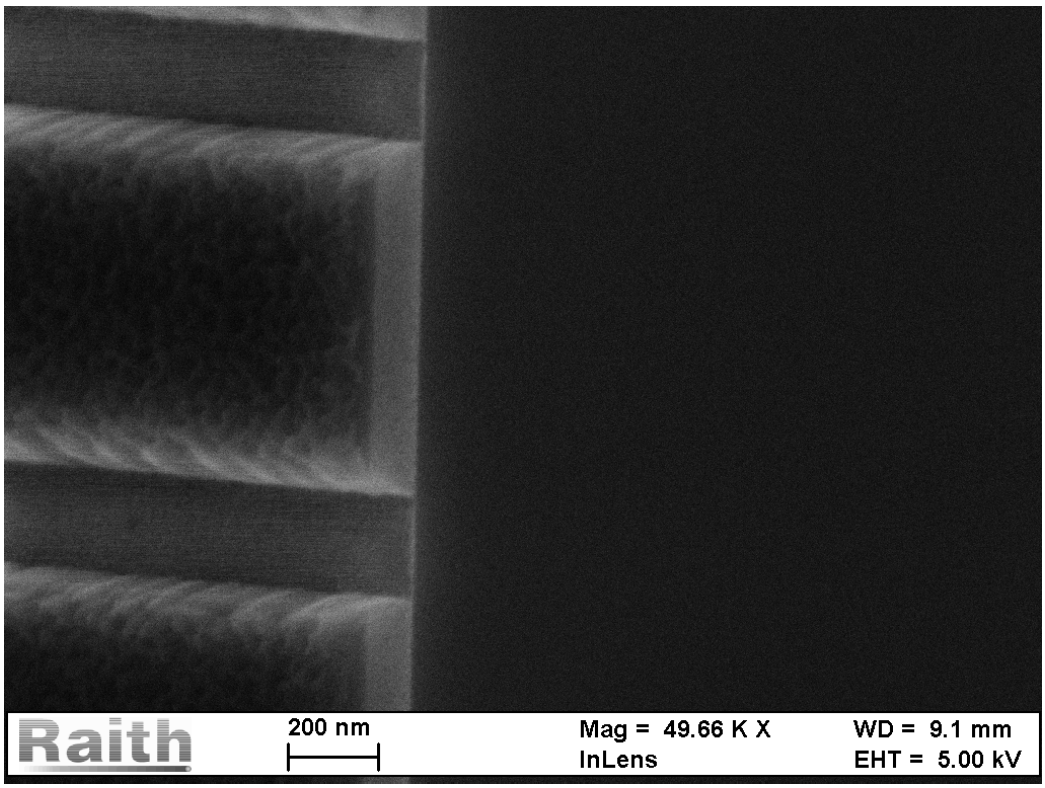

Figure 6.3: Succesful reactive ion etching of 200 nm lines in SiO_2 with a PMMA mask.
25 sccm Ar, 25 sccm CHF_3, 30 mTorr, 600 W, 6x30 seconds

6.2 Aluminium

6.2.1 Etching Aluminium

Using the etch rates specified by Transene, 75 °C was chosen as an initial etch temperature, with a specified etch rate of 55 nm/s. This would result in a etch time of 7 minutes and 35 seconds to etch through the 50 µm thick sample using double sided etching. However, the initial test sample experienced a violent reaction and was completely dissolved within 10 seconds. This is mainly due to the exothermic reaction of etching aluminium, as mentioned in section 3.5.1. For high temperatures, as in this case, the result is a positive feedback where extra heat increases the reaction rate, which in turn release more heat and so on, called a thermal runaway. This effect was further enhanced by the initial test being carried out in a small beaker and the increased surface available to the etchant with the entire back side of the sample exposed.

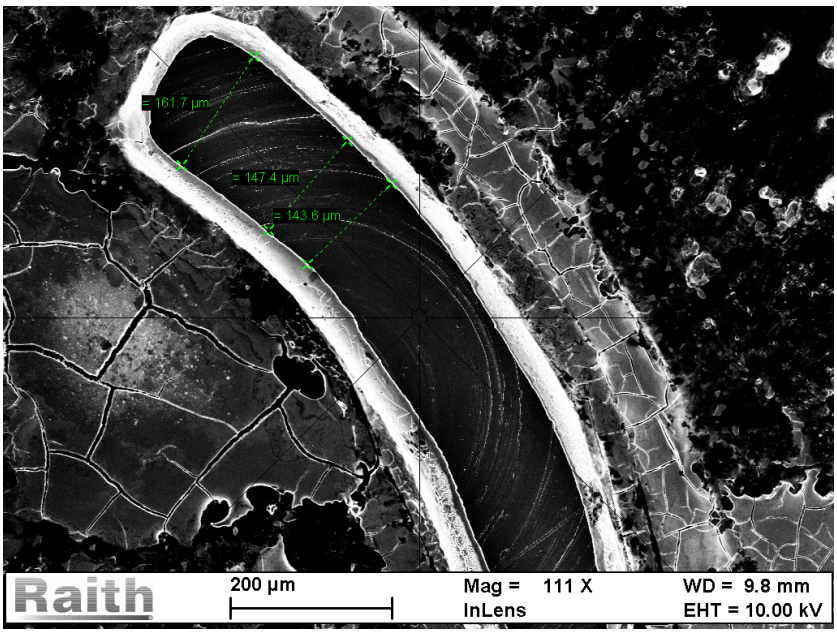

Figure 6.4: An initial attempt to pattern 125 µm and 5 µm wide arcs. The 5 µm arc can be seen as a the lighter region to the right of the large arc.

40 °C was settled on as a more appropriate etch temperature by etching aluminium foil pieces and comparing the total etch time to the rate specified by the manufacturer. A 15 µm thick aluminium foil was etched until completely dissolved, with a total etch time of approximately 16 minutes. This corresponds to a total etch rate of 7.8 nm/s with the specified etch rate at 40 °C being 8 nm/s. Factoring in the uncertainty of the foil thickness, this etch rate is acceptable and does not suffer from the same problems with thermal runaway as the reaction at 70 °C.

A pattern consisting of 125 µm and 5 µm thick lines and arcs, representing the largest and smallest open zones was used for testing the aluminium etchant. The exposed back of the wafer was still problematic and attempts at patterning with this setup resulted in large, uneven and over-etched patterns. Subsequent experiments used a protective SiO_2 layer on the bottom side.

Initial attempts used 30 nm SiO_2 on both sides of the substrate and 2x30 s of dry-etching for the pattern transfer into SiO_2, which can be seen in figure 6.4 and 6.5. The sample surface showed large areas covered by residue. This was believed to originate from the SiO_2 or the PMMA layer. The sample was subsequently cleaned with acetone to remove any PMMA residue, dry-etched with the SiO_2 recipe to remove excess SiO_2 and dry-etched with O_2 to remove possible organic polymers. This did not remove the residue.

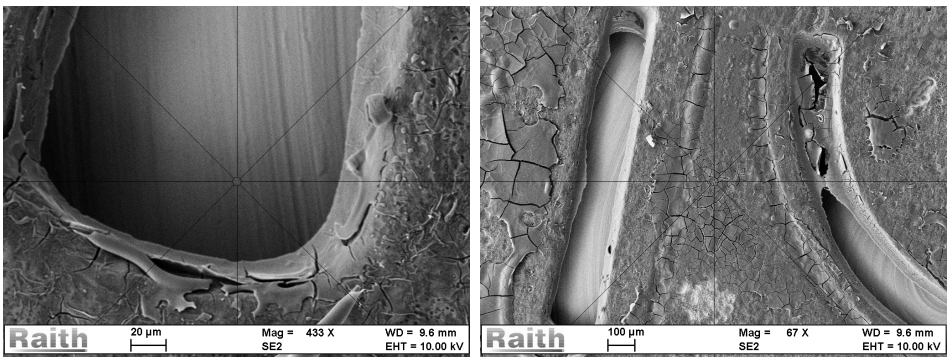

(a) (b)

Figure 6.5: These figures show the sample in figure 6.4 after the attempts at removing the surface residue. The residue still covers large areas of the sample and completely covers the 5 µm elements.

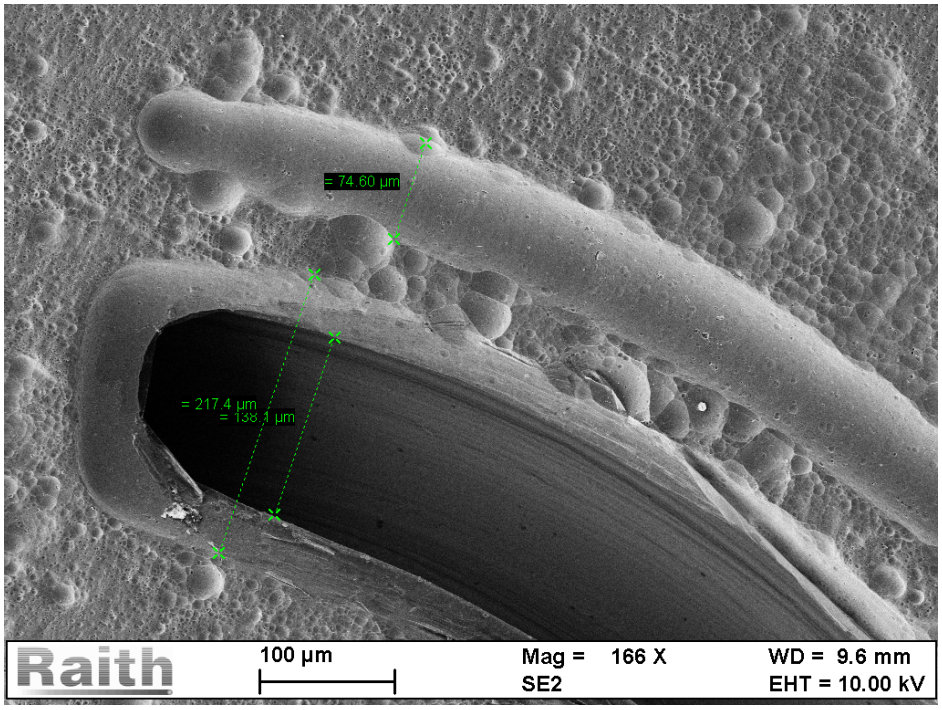

Figure 6.6: Results after removing PMMA prior to etching. This resulted in a significant overall improvement. The large arc has a more even curvature and has fully opened. The small features and surface pitting is still problematic.

After investigating the back side of the sample it was discovered that this side did not contain the same residue. The origin of the residue was later discovered to be the PMMA layer. After removing the PMMA with acetone

before etching the problem was solved. The exact composition of the residue and the mechanism of its formation remains unexplored.

The two major unresolved issues at this time was the surface pitting and the pattern dependent etch rates (large elements experiencing higher rates). The mask thickness was changed to 100 nm in an attempt to resolve the pitting problem.

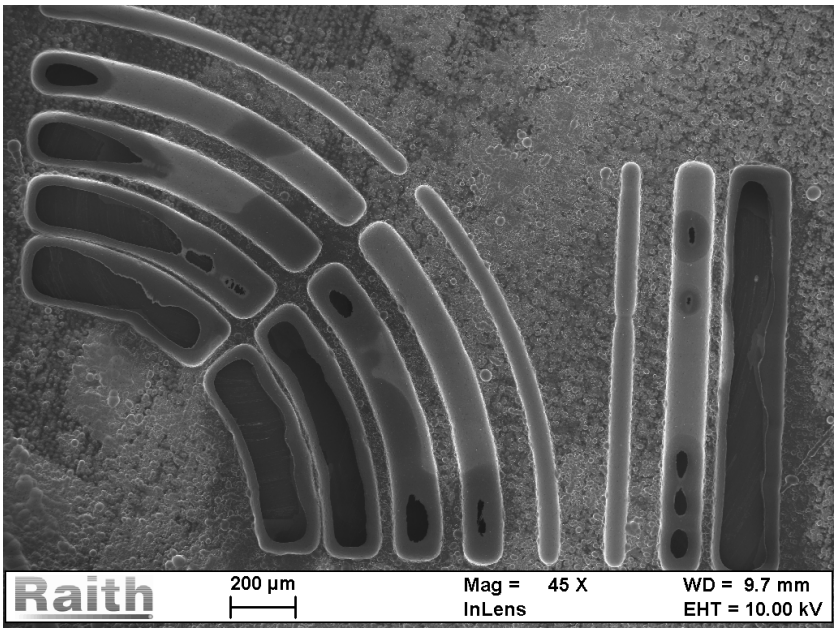

Figure 6.7: This figure shows the challenges faced with feature dependent etch rates. This sampled used a 100 nm SiO_2 mask, but surface pitting is still prevalent.

In figure 6.8 a long line can be seen cutting across the leftmost straight line. This is probably due to a large crack in the masking layer, allowing etchant underneath the layer, removing aluminium and eventually loss of contact between substrate and mask. This is also a likely cause of the pits observed in the narrow arc.

Although the splitting of lines in figure 6.8 reduced the etch rate, it was still too high compared to the narrow segments to pattern with the desired resolution. This is because the aluminium etch reaction is diffusion-based due to its exothermic nature[57].

The lack of mask integrity and the issues concerning narrow features was deemed to be insurmountable. A new perspective was necessary and some last effort attempts at aluminium patterning was made using two step processes. The pattern was first created using the standard settings and

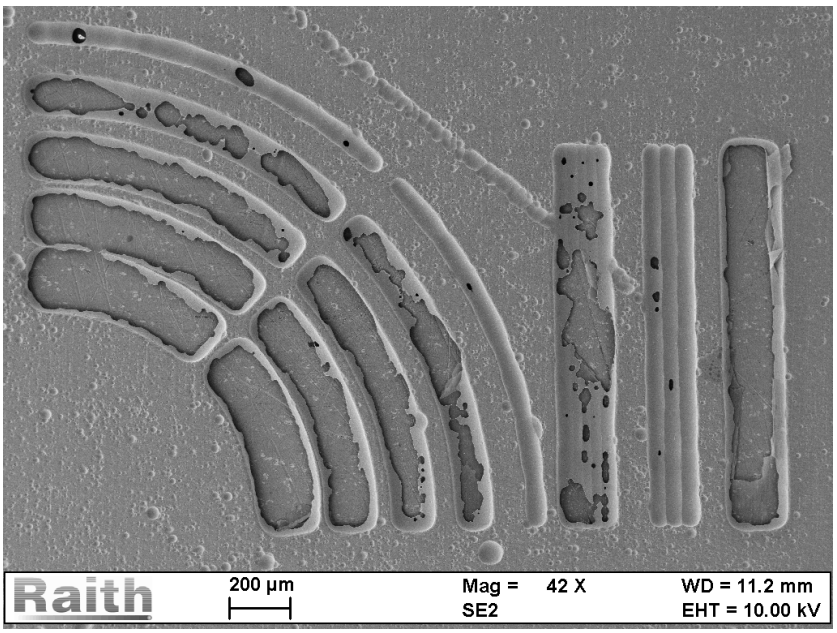

Figure 6.8: Over-etching sample to investigate the effect of splitting large patterns into thin lines. On the right side is an attempt to fabricate a 125 µm line using pattern adaption. A line was split into 5x5 µm, 3x5 µm and 1x125 µm lines in an attempt to achieve a feature independent etch rate. Significant pitting from the back side of the sample creates holes, even in narrow features.

etched to 10 µm depths on the front side. The sample was subsequently coated with 100 µm SiO_2 at 45° in an attempt to preserve the pattern under etching. Etching was then performed on the back side of the sample. This was unsuccessful and resulted in the complete disintegration of the sample, hence no pictures are available of this result.

6.2.2 Imaging Issues

Imaging issues with the aluminium samples occupied a considerable amount of time early on in the project. At that moment, the samples were being imaged using the previously mentioned PEEK sample holder, coated with AuPd to reduce charging. This manifested itself as an inability to achieve good images, low resolution and extreme stigmation values required to obtain even mediocre focus. Even maximum stigmation compensation was insufficient.

Charging of the sample holder was initially suspected to be the cause of this. Consequently it was sputter coated and alumninium foil was placed under sample and at the clamps securing the holder to the SEM to ensure

conductivity, but the issues persisted.

Later, this was found to in fact be due to charging of the sample holder, presumably mainly from the screws which were too small for the AuPd sputter coater. This realization came after noticing the required stigmation direction varied with position on the sample. After the PEEK has acquired a negative charge, it will deflect the beam away from the sample holder edge. This leads to an elliptical beam shape, even more than the beam-column can compensate for.

6.3 Chromium Zone Plate

The chromium zone plates used the same pattern and EBL-process used to fabricate zone plates in silicon to ensure comparable results. These were destined to be illuminated with a laser in order to verify the pattern, outlined in section 4.2.

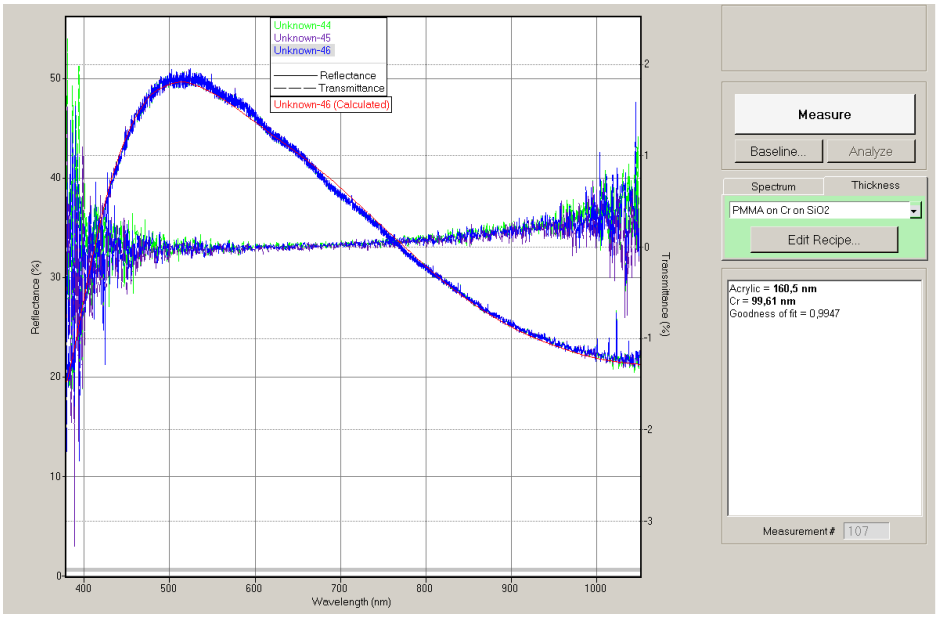

Figure 6.9: Measured thickness of the chromium film and the PMMA resist using a Filmetrics F-10 thin film analyzer. The Cr film was measured to 100±2 nm and the PMMA 160±2 nm.

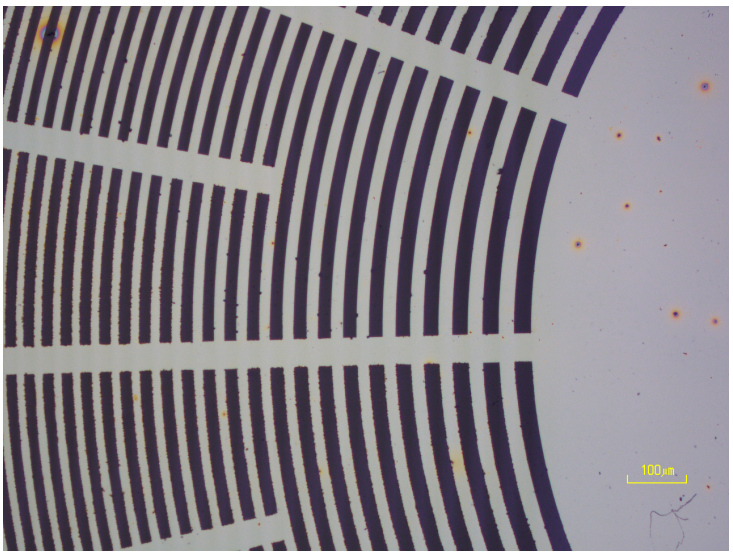

Figure 6.10: Optical reflective micrograph of the chromium zone plate. The dark is areas where the chrome layer has been removed.

6.4 Reactive Ion Etching Silicon Nitride

After carrying out the same adaptation procedure used for reactive ion etching of SiO_2, the necessary RF-power was found to be 450 W for the nitride recipe. By measuring the thickness inside the pattern compared to the area still covered by PMMA, the total etch depth was found to be 65 nm, hence an etch rate of approximately 22 nm/min. The PMMA showed similar etch rates during this etching, varying by distance to pattern openings.The maximum PMMA etch rate was found on the edge of the pattern as 27 nm/min. The results can be seen in figure 6.11

6.5 Silicon Substrates

6.5.1 Silicon Membranes

Initial etching experiments used a holder in which the wafers were etched standing upright. This practice was later abandoned due to a temperature gradient in the etch solution, with the solution being colder further up. This led to etch depths varying by as much as 35 µm across a membrane for a 460 minute etch. The measured etch rate for samples standing up were ~1.1 µm/min. For wafers etched flat on the PTFE holder, the depths were mainly measured using the working distance method. Observed etch rate

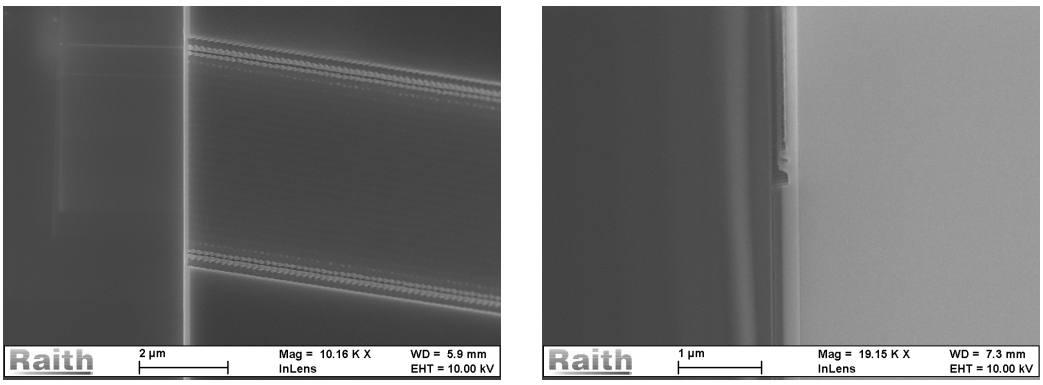

(a) 45° view of 5 µm line. (b) Cross section view of 5 µm line.

Figure 6.11: Results after adapting reactive ion etching of silicon nitride. The noticeable hills are due to problem with the EBL exposure. The hills are situated along the edge of the line, indicating dose problems. The central area of the line will have dose contributions from forward scattering electron originating in neighboring areas, increasing the received dose. This sample was exposed during a period of several equipment issues concerning the e-LiNE, which may also have played a role.

on this holder was significantly lower, 0.8 µm/min. The author speculates that this can be explained by the larger flat holder forcing the solution to flow further up the sides from the bottom of the beaker to cool down before interacting with the membrane surface (facing upwards), resulting in a lower effective etchant temperature.

6.5.2 Silicon Zone Plate

Figure 6.14-6.18 shows an attempt at making a 5 µm thick silicon zone plate. The membrane thickness for this sample is thus 10 µm. The pattern was written using a 60 µm aperture and 50 nm step size before being developed and dry-etched for 14 minutes. (110) is oriented along the bottom of the figure for all pictures.

The zone plate was later etched until the zones were open. Unfortunately this destroyed the most of the silicon edges intended for diffraction. However, this revealed the resilience of the nitride layer, which can be seen in figure 6.19.

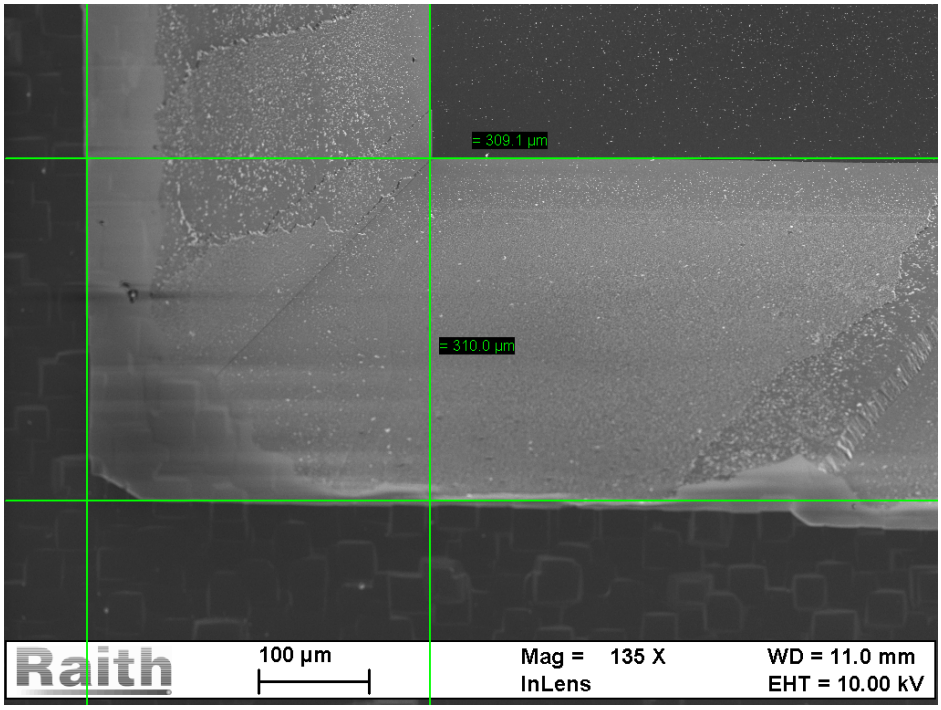

Figure 6.12: Example showing depth measurements in the process of making a silicon membrane. The measured depth here is $310 \times \sqrt{2} = 438\,\mu\text{m}$

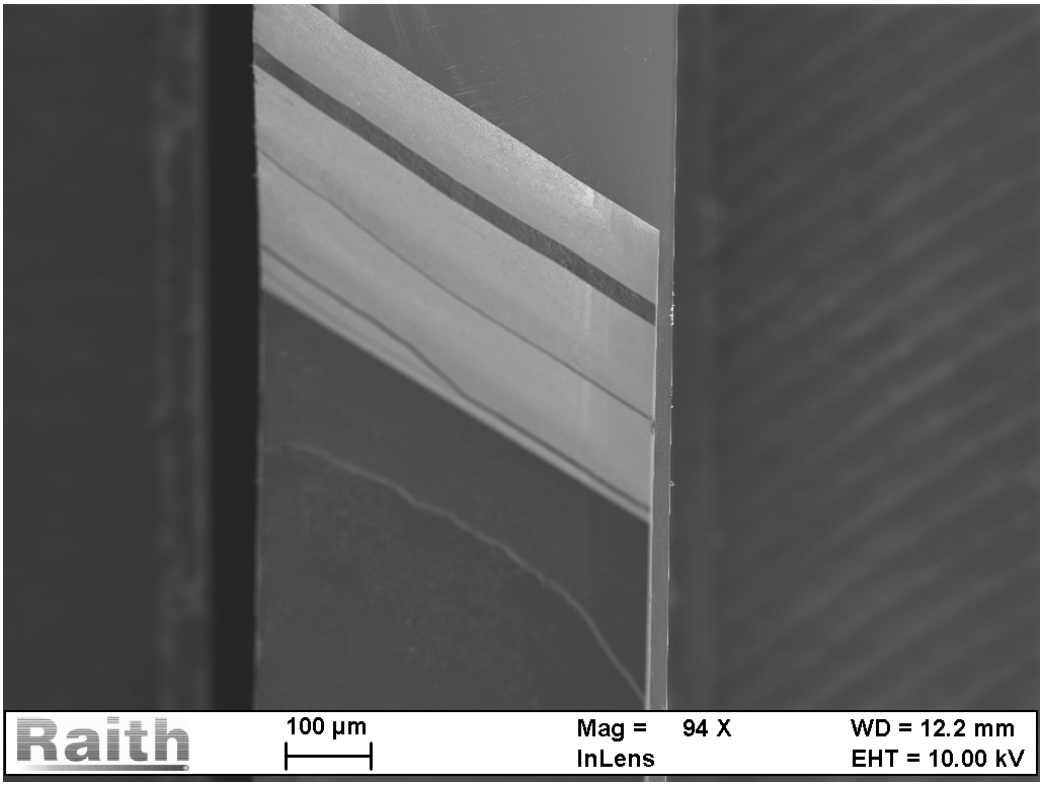

Figure 6.13: Cross section of a silicon membrane. This membrane was rejected due to the issues concerning uneven etch rates. The image is taken using high current mode and a small aperture, resulting in a large depth of field.

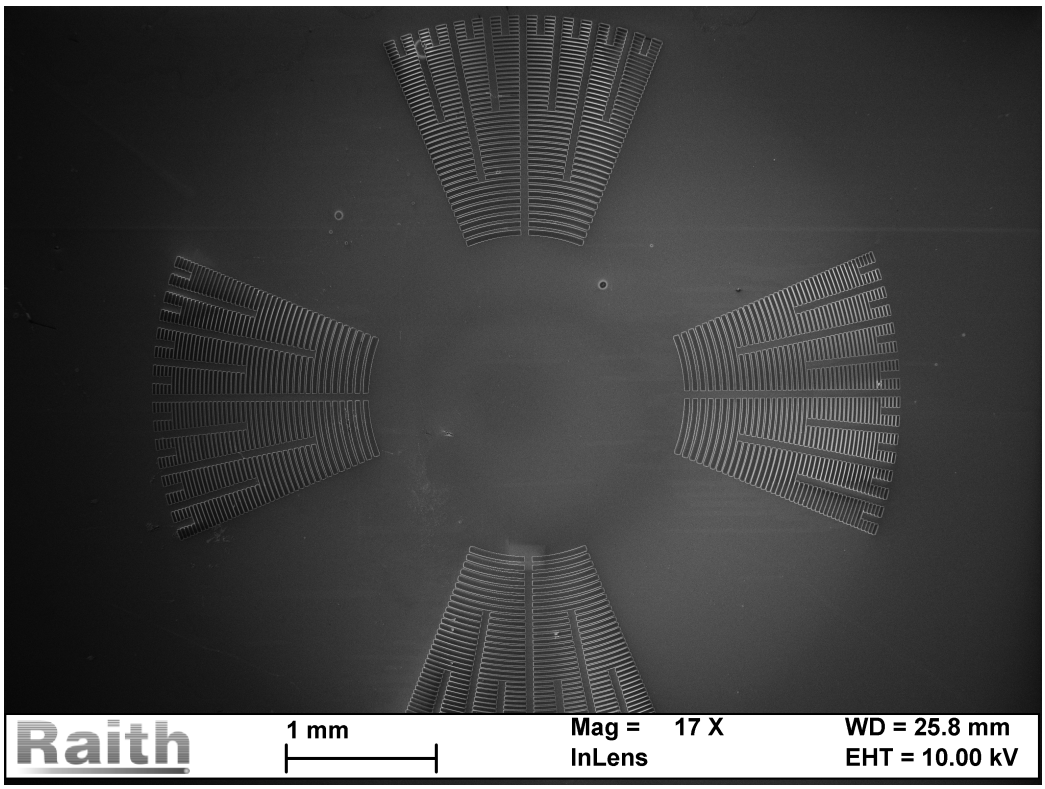

Figure 6.14: Overview of the patterned area in an attempt to make a 5 µm thick zone plate. The etch depth here is 3 µm.

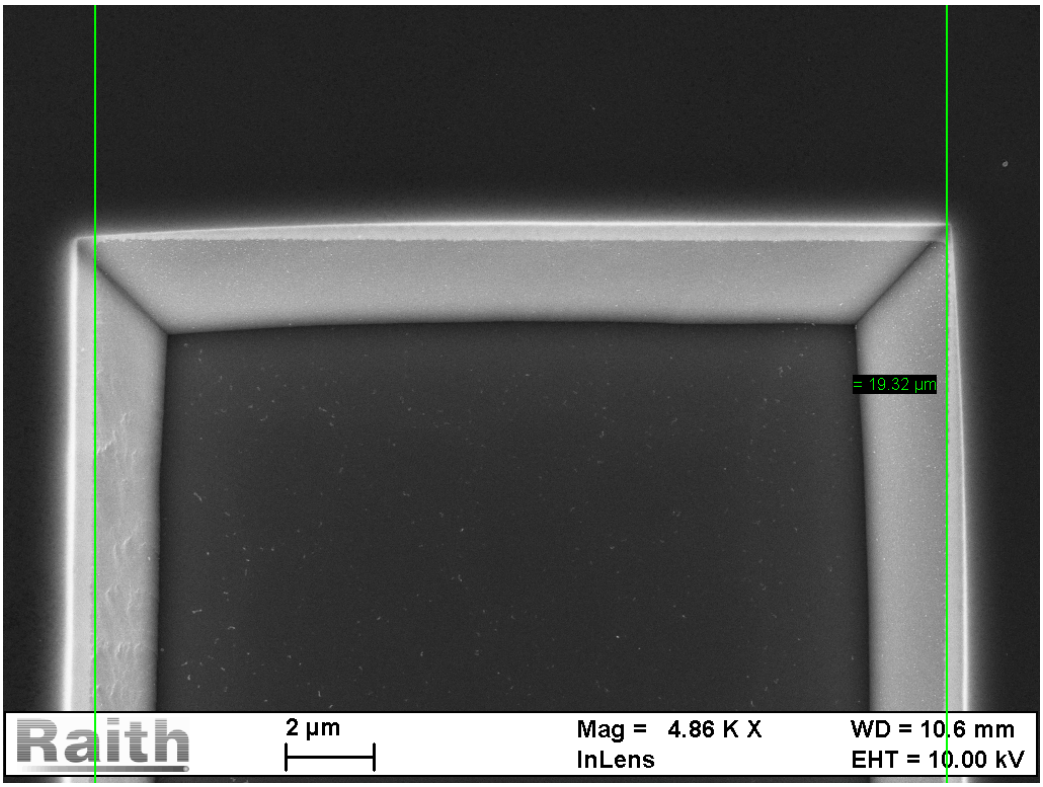

Figure 6.15: Outer zone of the 3 µm deep pattern. Pattern-width of this zone was 19.26 µm, i.e. a 0.3% deviaton. Considering this was patterned using a step size of 50 nm, this is very close to the an optimal result.

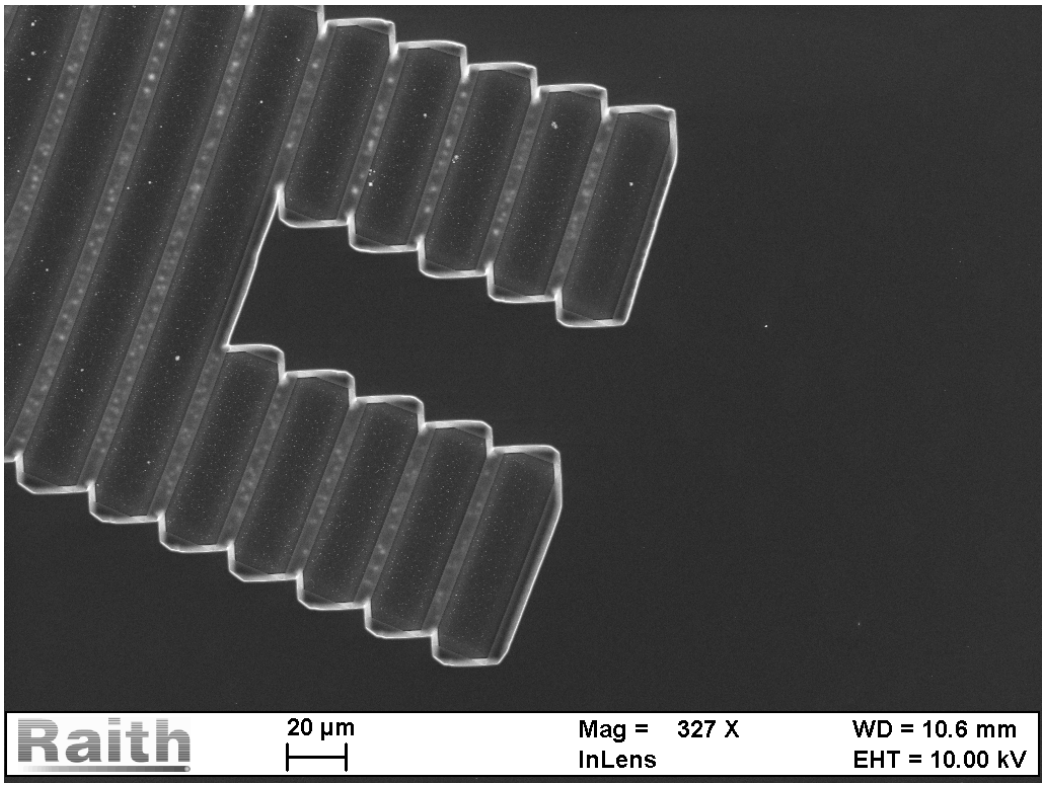

Figure 6.16: This figure shows the effects of having openings tilted. The zones are overlapping and only a small amount of silicon is left underneath the blocked zones.

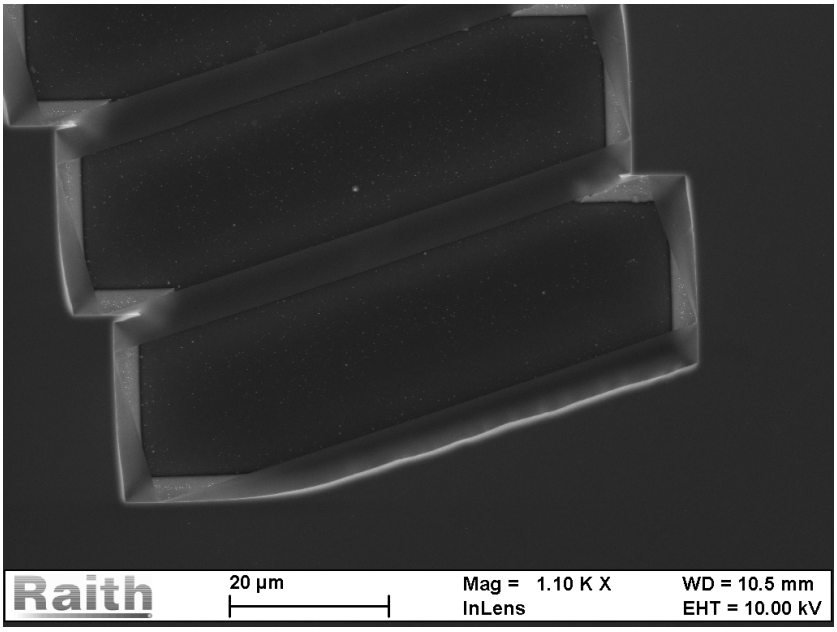

Figure 6.17: After an etch depth of 4 µm, the tilted zones have fully overlapped, leaving only nitride hanging between the support bars. Note the already developed smooth surface underneath the nitride.

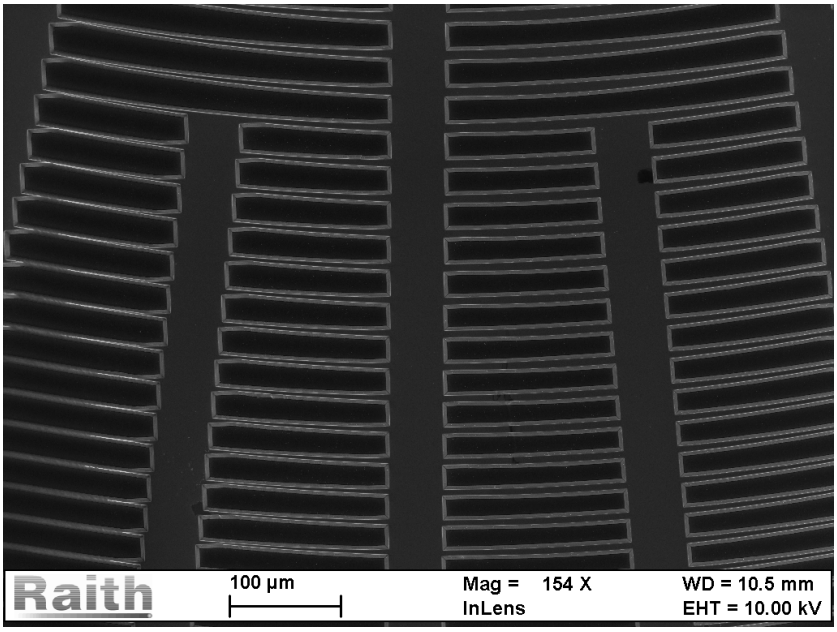

Figure 6.18: Etch depth is 5 µm, but the zones are still not open, meaning the membrane was too thick before etching.

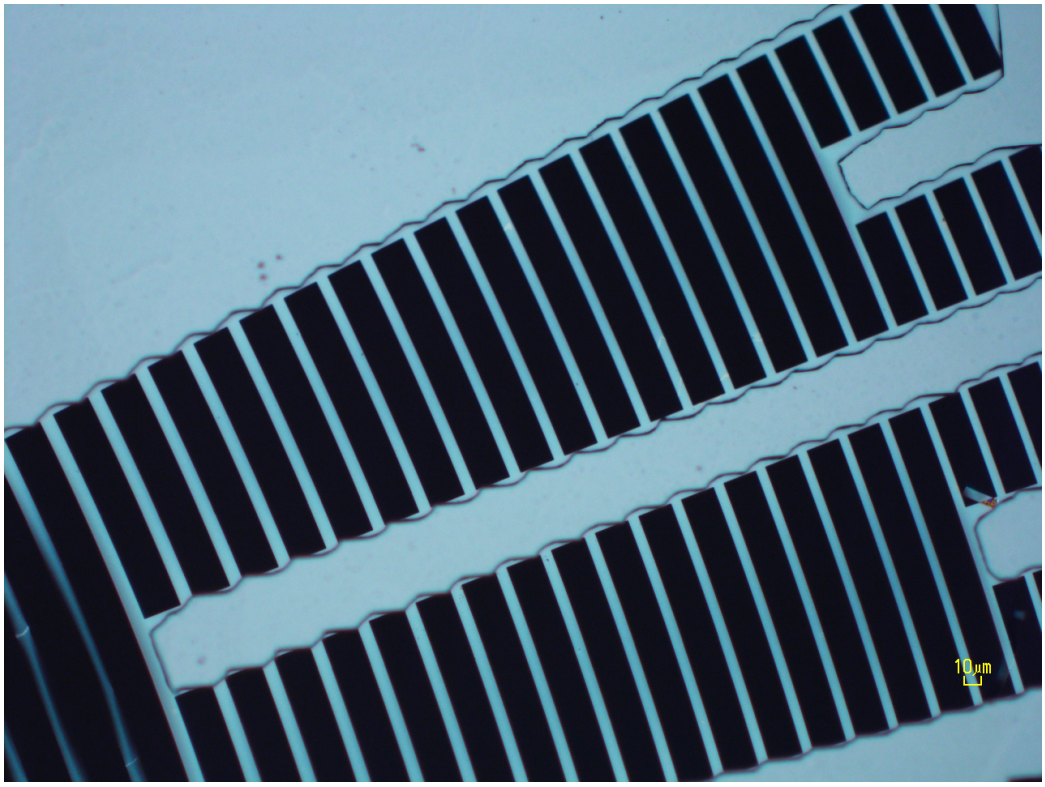

Figure 6.19: Optical micrograph from the backside of the sample after etching until completion. The support bars from the membrane are still intact, while the wide sections are buckling under their own weight. Other sections of the zone plate had greater damage.

6.6 Successful Fabrication of a Silicon Nitride Zone Plate

Figure 6.20-6.24 shows the initial attempts at fabricating a silicon nitride zone plate using the rotated pattern. This used a $\frac{length}{width}$-factor of 20, which proved to be inadequate to support some of the inner zones, see figure 6.23. From a total of 1184 individual openings, 6 were found to be damaged, which can be seen in figure 6.23 and 6.24 (b). This factor was later reduced to 14 to allow for the secondary support bars to extend into the central stop. With a support factor of 14, not a single broken element was found.

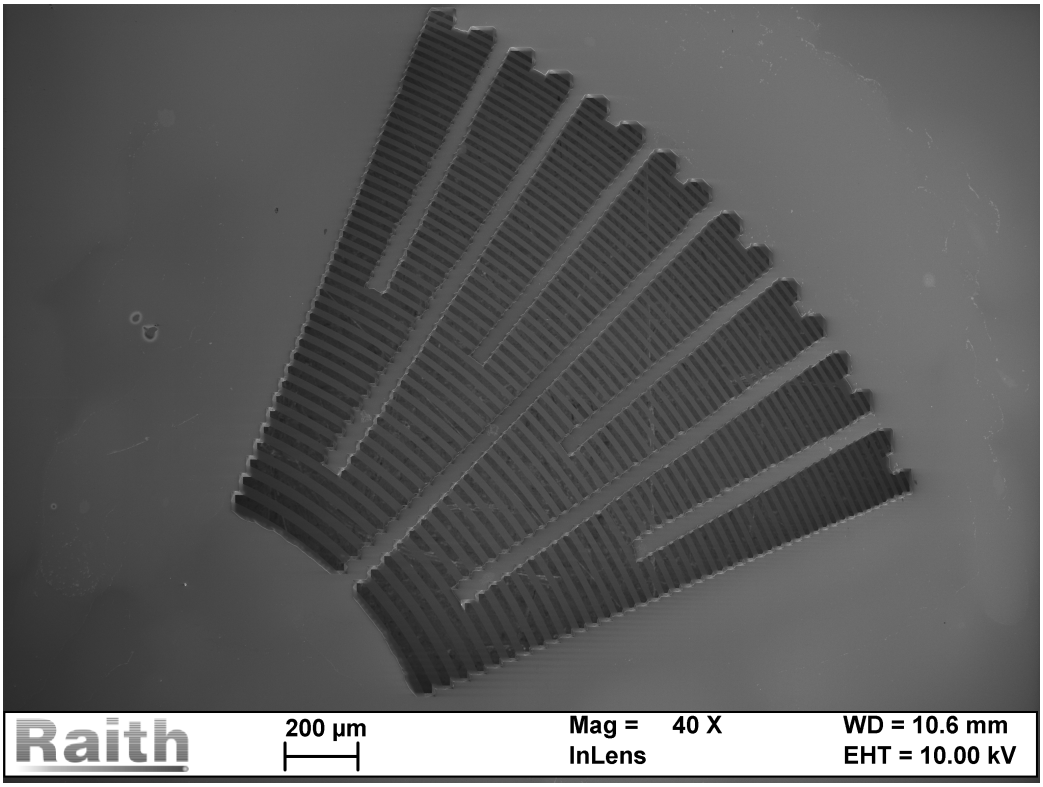

Figure 6.20: Overview of the top right quarter of the first silicon nitride zone plate fabricated. Scratches in the SEM sample holder is visible through the open zones.

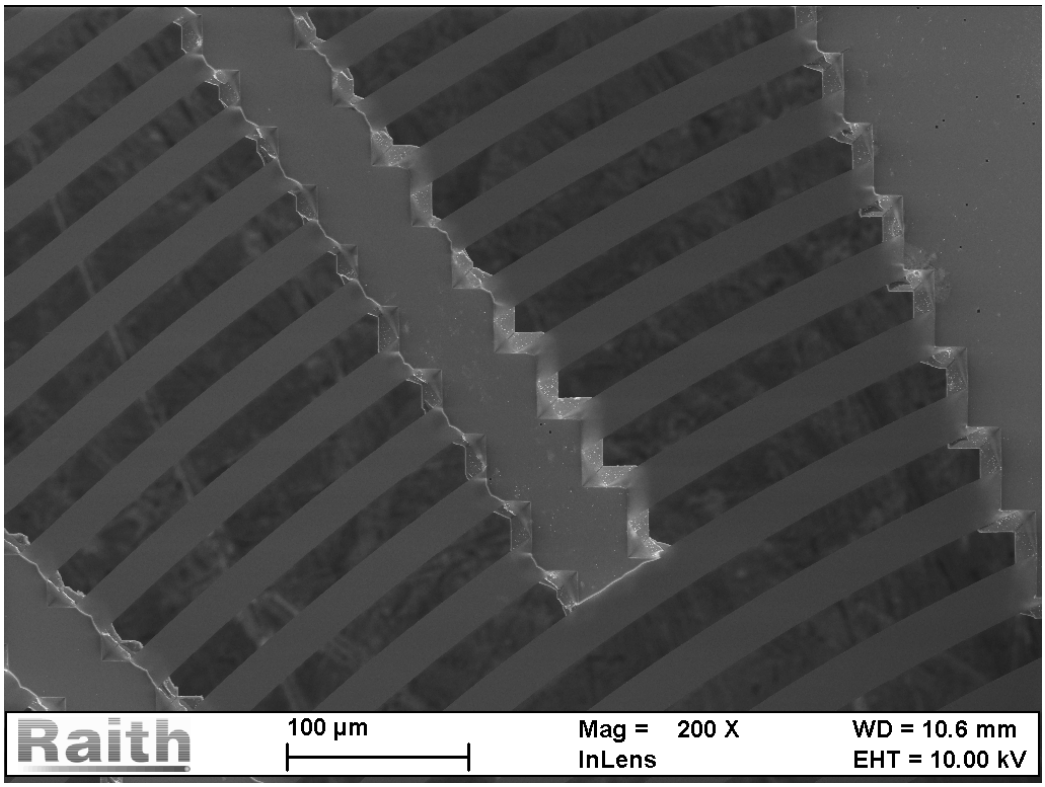

Figure 6.21: The interface between the open zones and the support bars. The zig zag pattern is created due to every open zone creating its own square and exposing two (111) planes, ceasing further etching into the support bar.

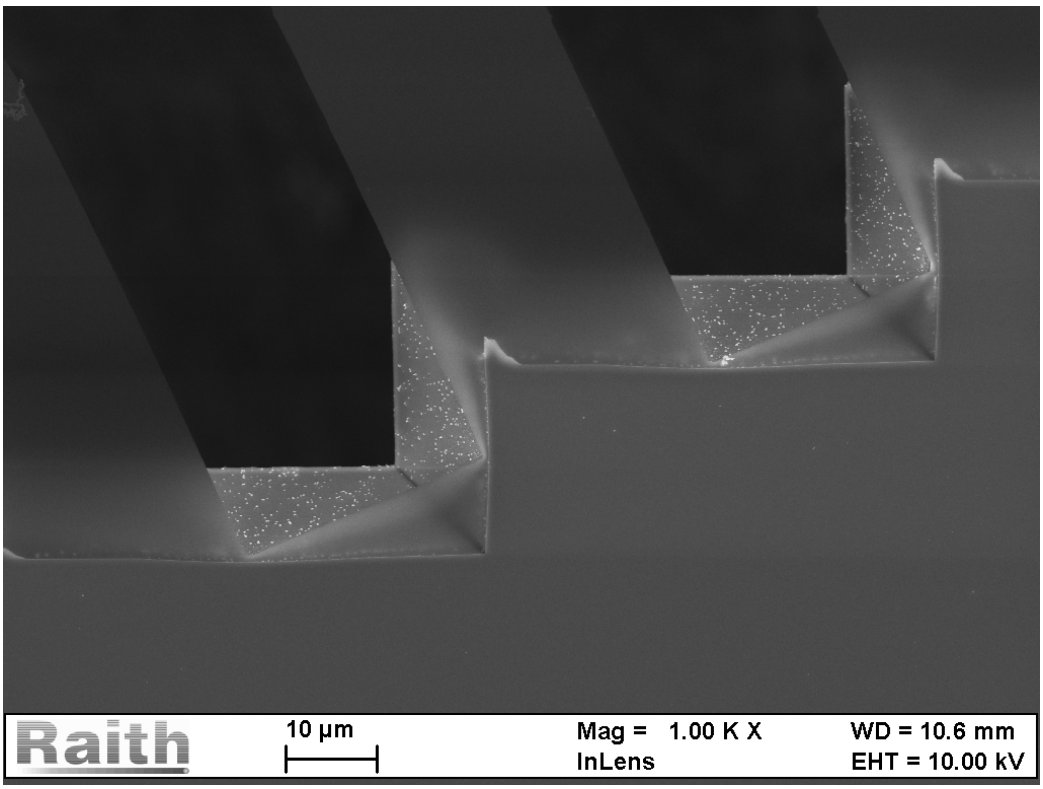

Figure 6.22: A detailed look at the transition between free-standing nitride and the support bar.

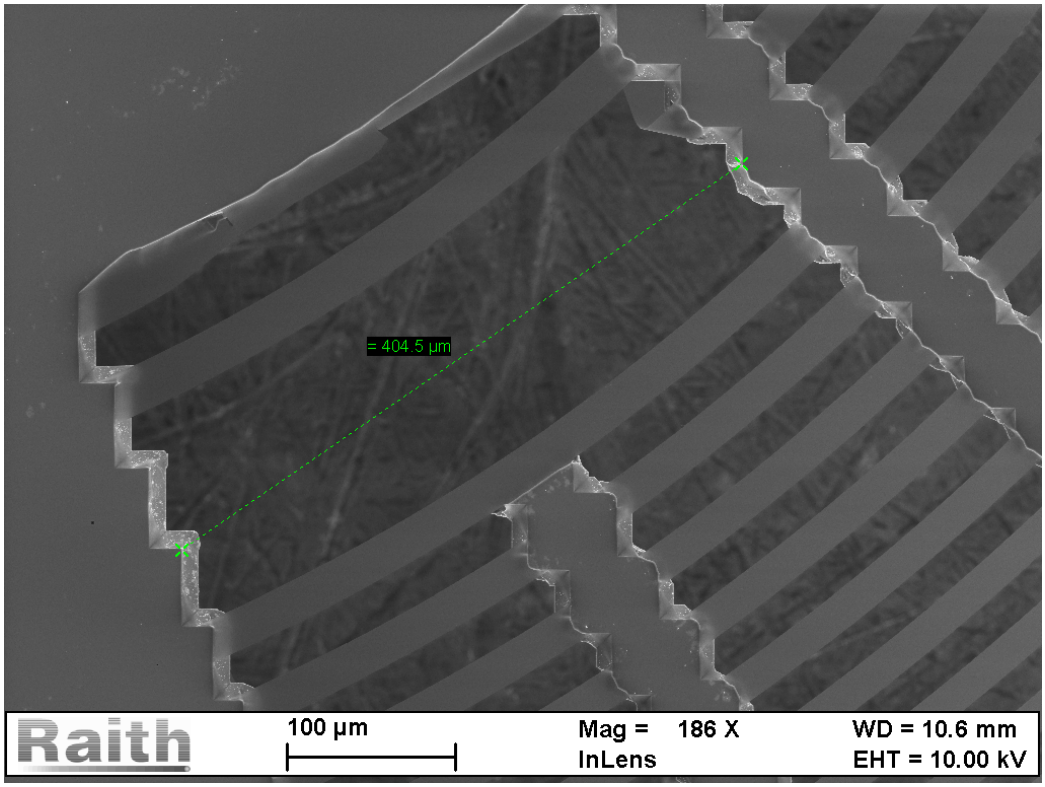

Figure 6.23: The inner zone of a damaged quarter. The intact element is spanning a 350 µm gap.

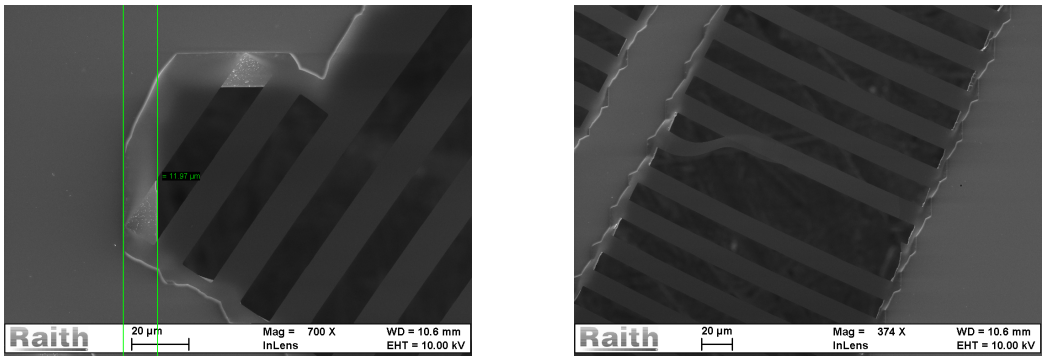

(a) (b)

Figure 6.24: (a) the thickness measurement of the underlying silicon membrane, here 16.9 µm
(b) a broken nitride element, adhering to the closest neighbour.

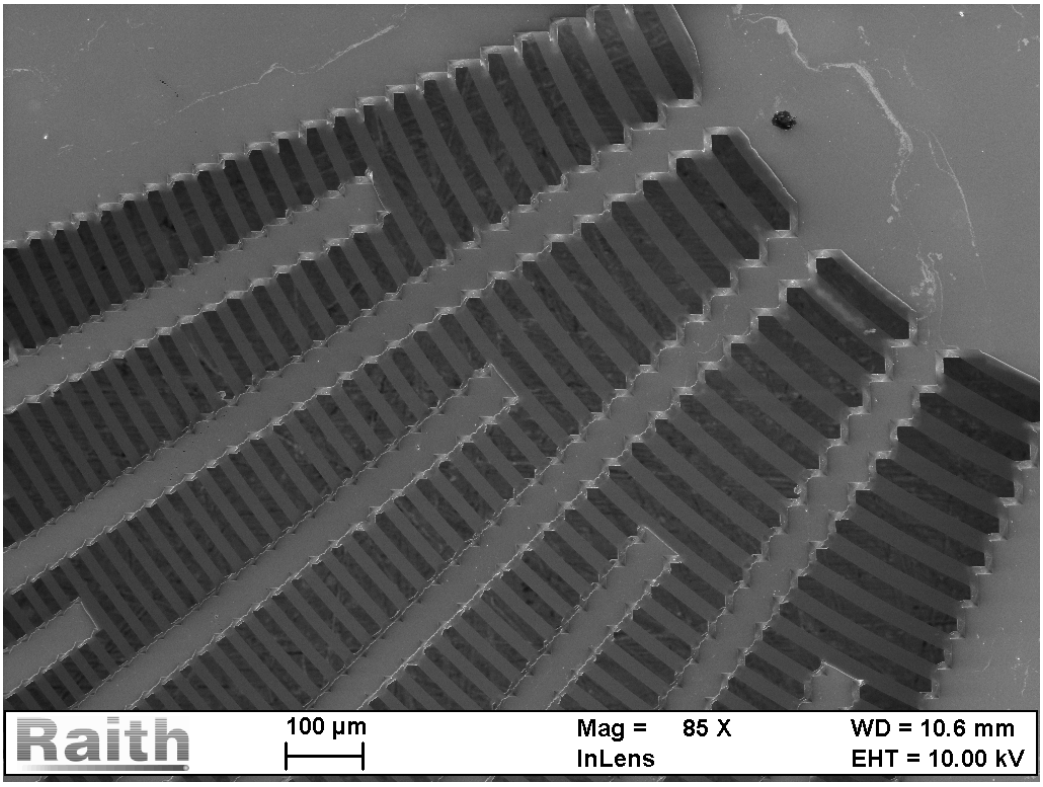

Figure 6.25: Inner zones of the zone plate fabricated using a support factor of 14. The buckling problem shown in figure 6.23 is now avoided. Some residual silicon can be seen under one of the innermost zones, but this will not affect the performance of the zone plate.

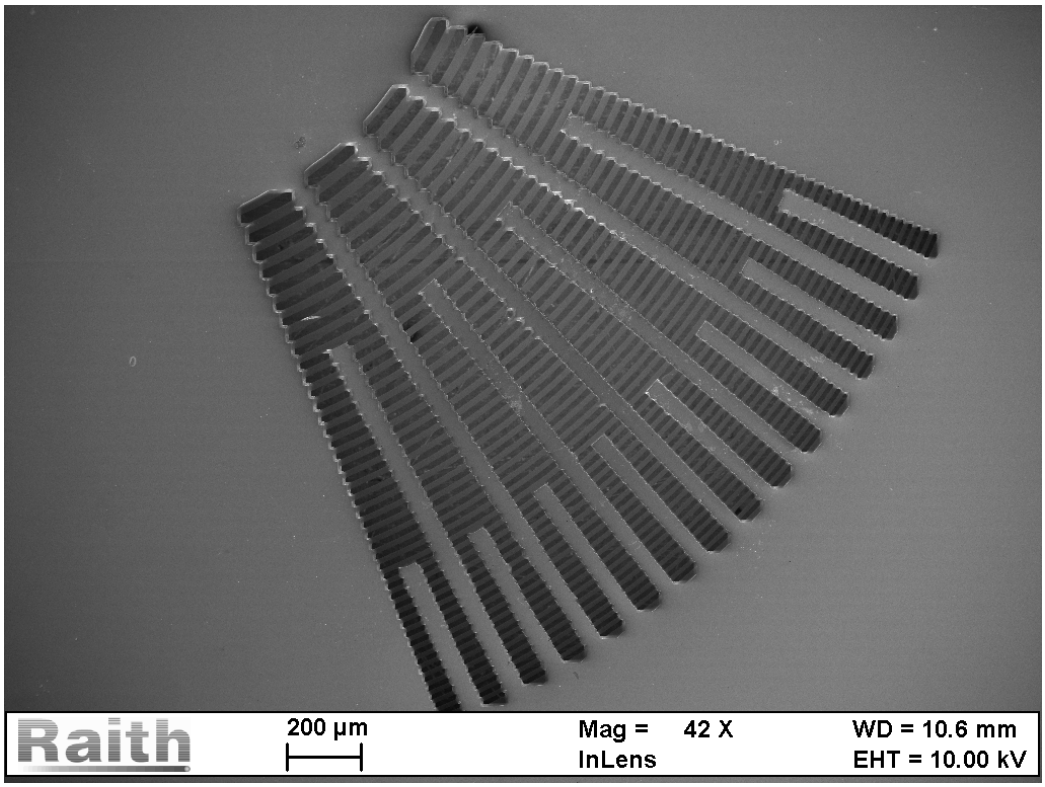

Figure 6.26: Overview of one quarter of the zone plate using support factor 14. Every quarter now has three support bars extending into the central stop. The underlying silicon layer was measured to be 13.1 µm.

6.6.1 Optical Measurements

The partially damaged zone plate created using support-factor 20 was tested using the optical setup. Due to time limitations it was not possible to do further optical tests on other zone plates. A chromium zone plate with an identical pattern was used for comparison. The chromium zone plate shows a spot intensity four times higher than the silicon nitride. This is attributed to the blocked zones of the nitride not being fully opaque which will lead to destructive interference from the blocked zones, reducing the focal spot intensity. Due to resolution limitations of the detector, the true resolution could not be measured. But for this detector, every pixel covers a 5.2 µm square. From figure 6.27, the half intensity point can be found one pixel away(left side) from the maxima but is not visible on the right side. This means the FWHM and the resolution of the zone plate is 10-15 µm, corresponding well to the theoretical resolution of 12 µm from the width of the smallest zone, see section 2.1.1.

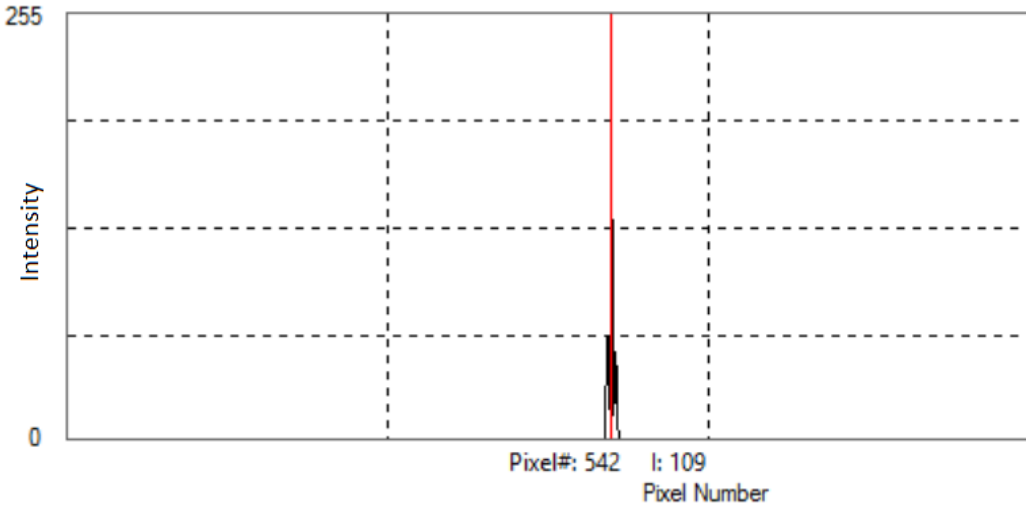

(a)

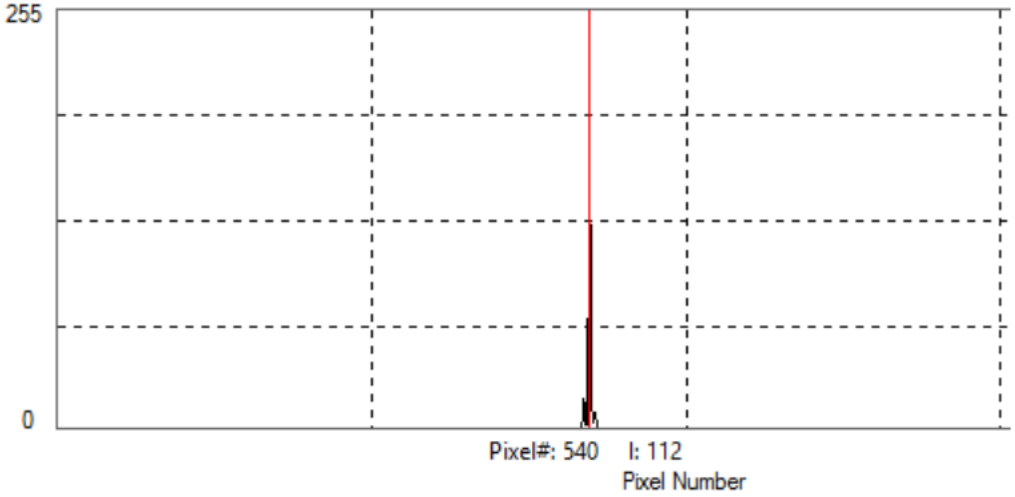

(b)

Figure 6.27: This figure shows an intensity comparison between a silicon nitride and a chromium zone plate with identical patterns.
(a) shows the measured intensity of the silicon nitride zone plate with a laser output power of 557 µW. The peak intensity is at 109, covering one pixel.
(b) shows the intensity a chromium zone plate with identical pattern. The detector settings are identical to (a), but the laser power has been adjusted to 145 µW. This yields the same focal point intensity, with peak intensity at 112.

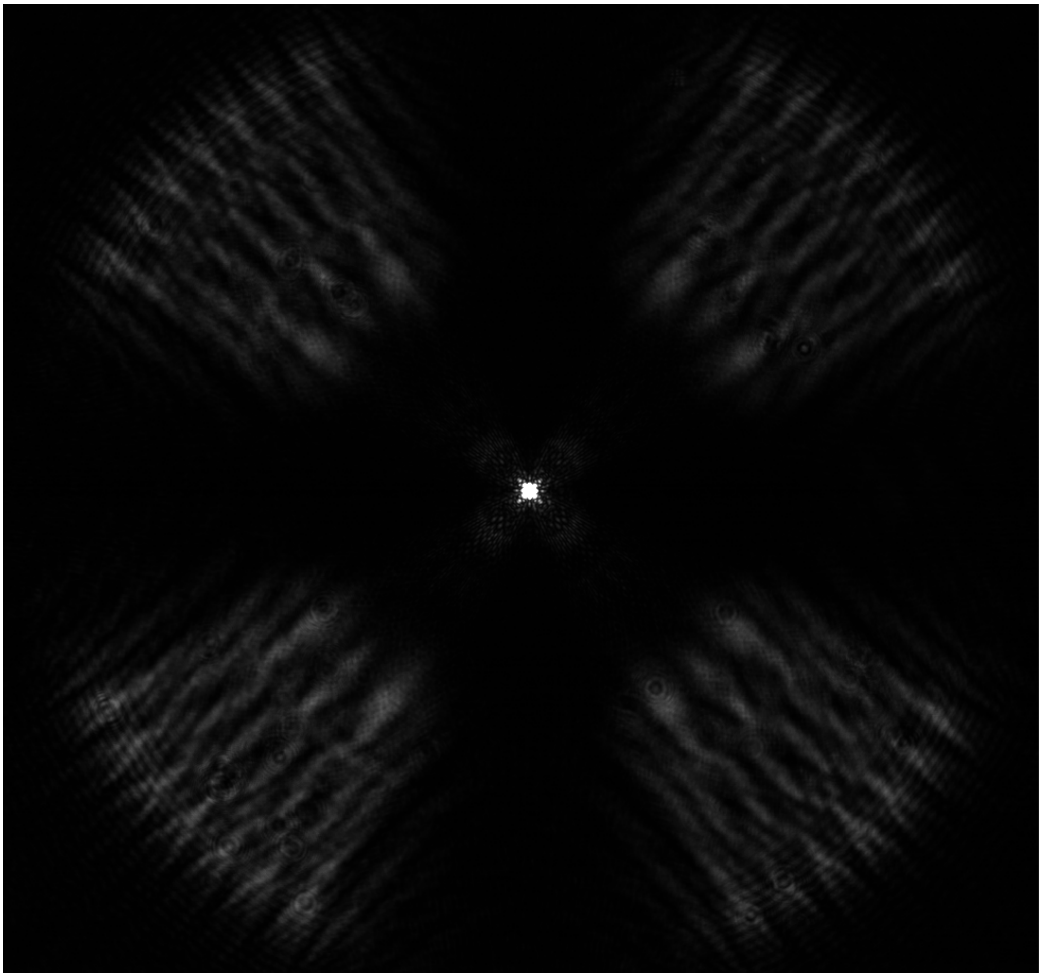

Figure 6.28: First order focal spot of the silicon nitride zone plate. The zero order beam can be seen as the large grey areas outlining the open zones. The second order focus is also visible, surrounding the first order focal spot, not yet in focus. This was taken using a high exposure time, to show the various elements. This also leads to the focal spot covering multiple pixels due to saturation.

Chapter 7

Conclusions and Future Work

The objective of this thesis was to fabricate free-standing Fresnel zone plates for focusing a Bose-Einstein condensate of metastable helium atoms with a wavelength of 100 nm. The zone plate was designed to have a focal length of 60 cm to fit the experimental setup in the group of Prof. Zeilinger at the University of Vienna.

After attempting this with aluminium and silicon, this was finally realized using a silicon membrane with silicon nitride serving as the diffraction surface. The zone plate has 42 zones, a 2 mm central stop and a diameter of 5 mm. To the best of our knowledge this is >100 times larger than any previously fabricated free-standing zone plate ever made in this group or elsewhere.

In the process of patterning these materials, several new procedures has been introduced to the UiB NanoStructures laboratory. During this thesis, dry-etching of SiO_2 using a PMMA mask, dry-etching of silicon nitride without the need for secondary layers, aluminium wet etching and the fabrication of silicon membranes has been realized for the first time at the facilities. Methods for quantitatively etching silicon has also been established.

Now that the necessary fabrication process has been established, it can be extended. Larger patterns should be possible, as well as writing several zone plates per wafer, enabling larger patterns with more zones. This will simplify pattern placement and decrease fabrication time. To enable this, a custom mask for the photolithography step would be necessary, which could be patterned in chromium on SiO_2, similar to the chromium zone plates produced.

In a RIE-system equipped for deep reactive ion etching using e.g. SF_6+C_4F_8 called the Bosch process, the final step could be performed on the fabricated membranes without the need for blocking circular arcs, thereby doubling the

transmissivity of the zone plates. A typical example of this process is shown by Fan et al, achieving aspect ratios of 20:1 in silicon[58]. This would also avoid the zig zag pattern along the interface between open zones and support bars.

Another possible idea is to create a zone plate consisting of two different patterns, one with a long focal length and one with a short. By tuning the 3rd order focal length of the former to match the 1st order of the latter one, the zone widths of the inner and the outer most zone will differ less. This technique has been utilized by Chao et al. to create lenses for x-ray imaging with 12 nm resolution[59].

Hopefully, the zone plates created as a part of this thesis may some day be used in the aforementioned BEC matter wave experiments to further the understanding of this state of matter.

Bibliography

[1] L. De Broglie, "Recherches sur la théorie des quanta", PhD thesis, Migration-université en cours d'affectation, 1924.

[2] G. P. Thomson and A. Reid, "Diffraction of cathode rays by a thin film", *Nature*, vol. 119, no. 3007, p. 890, 1927.

[3] I. Estermann and O. Stern, "Beugung von molekularstrahlen", *Zeitschrift für Physik*, vol. 61, no. 1, pp. 95–125, Jan. 1930, ISSN: 0044-3328.

[4] M. Arndt, O. Nairz, J. Vos-Andreae, C. Keller, G. van der Zouw, and A. Zeilinger, "Wave-particle duality of c-60 molecules", *Nature*, vol. 401, no. 6754, 680–682, 1999.

[5] S. Eibenberger, S. Gerlich, M. Arndt, M. Mayor, and J. Tuxen, "Matter-wave interference of particles selected from a molecular library with masses exceeding 10 000 amu", *Phys. Chem. Chem. Phys.*, vol. 15, pp. 14 696–14 700, 35 2013.

[6] J. A. Leavitt and F. A. Bills, "Single-slit diffraction pattern of a thermal atomic potassium beam", *American Journal of Physics*, vol. 37, no. 9, pp. 905–912, 1969.

[7] S. Eder, T. Reisinger, M. Greve, G. Bracco, and B. Holst, "Focusing of a neutral helium beam below one micron", *New Journal of Physics*, vol. 14, no. 7, 2012.

[8] S. D. Eder, A. K. Ravn, B. Samelin, G. Bracco, A. S. Palau, T. Reisinger, E. B. Knudsen, K. Lefmann, and B. Holst, "Zero-order filter for diffractive focusing of de broglie matter waves", *Phys. Rev. A*, vol. 95, p. 023 618, 2 Feb. 2017.

[9] T. Reisinger, "Free-standing, axially-symmetric diffraction gratings for neutral matter-waves: Experiments and fabrication", PhD thesis, University of Bergen, 2011.

[10] S. D. Eder, X. Guo, T. Kaltenbacher, M. M. Greve, M. Kallaene, L. Kipp, and B. Holst, "Focusing of a neutral helium beam with a photon-sieve structure", *Physical review A*, vol. 91, no. 4, 2015, ISSN: 1050-2947.

[11] D. Maclaren, B. Holst, D. Riley, and W. Allison, "Focusing elements and design considerations for a scanning helium microscope (shem)", *Surface Review and Letters*, vol. 10, no. 2-3, 249–255, 2003.

[12] J. C. Weaver and J. G. King, "The molecule microscope: A new instrument for biological and biomedical research", *Proceedings of the National Academy of Sciences of the United States of America*, vol. 70, no. 10, pp. 2781–2784, 1973.

[13] R. B. Doak, R. E. Grisenti, S. Rehbein, G. Schmahl, J. P. Toennies, and C. Wöll, "Towards realization of an atomic de broglie microscope: Helium atom focusing using fresnel zone plates", *Phys. Rev. Lett.*, vol. 83, pp. 4229–4232, 21 Nov. 1999.

[14] M. Koch, S. Rehbein, G. Schmahl, T. Reisinger, G. Bracco, W. E. Ernst, and B. Holst, "Imaging with neutral atoms—a new matter-wave microscope", *Journal of Microscopy*, vol. 229, no. 1, pp. 1–5, 2008, ISSN: 1365-2818.

[15] B. Holst and W. Allison, "An atom-focusing mirror", *Nature*, vol. 390, no. 6657, pp. 244–244, Nov. 1997, ISSN: 0028-0836.

[16] K. Fladischer, H. Reingruber, T. Reisinger, V. Mayrhofer, W. E. Ernst, A. E. Ross, D. A. MacLaren, W. Allison, D. Litwin, J. Galas, S. Sitarek, P. Nieto, D. Barredo, D. Farías, R. Miranda, B. Surma, A. Miros, B. Piatkowski, E. Søndergård, and B. Holst, "An ellipsoidal mirror for focusing neutral atomic and molecular beams", *New Journal of Physics*, vol. 12, no. 3, p. 033 018, 2010.

[17] M. Keller, M. Kotyrba, F. Leupold, M. Singh, M. Ebner, and A. Zeilinger, "Bose-einstein condensate of metastable helium for quantum correlation experiments", *Physical Review A*, vol. 90, no. 6, pp. 063607-1–063607-9, 2014.

[18] M. Leduc and C. Cohen-Tannoudji, "Ultracold metastable helium: From atoms to exotic molecules", *Laser Physics*, vol. 20, no. 1, pp. 13–22, Jan. 2010.

[19] T. Judd, R. Scott, G. Sinuco, T. Montgomery, A. Martin, P. Krüger, and T. Fromhold, "Zone-plate focusing of bose–einstein condensates for atom optics and erasable high-speed lithography of quantum electronic components", *New Journal of Physics*, vol. 12, no. 6, p. 063 033, 2010.

[20] A. G. Michette, *Optical systems for soft X rays*. Springer, 1986, ISBN: 978-1-4612-9304-0.

[21] E. Hecht, *Optics*. Pearson, 2016, ISBN: 9781292096933.

[22] S. Rehbein, "Entwicklung von freitragenden nanostrukturierten zonenplatten zur fokussierung und monochromatisierung thermischer heliumatomstrahlen", PhD thesis, Göttingen, 2001.

[23] G. W. Webb, I. V. Minin, and O. V. Minin, "Variable reference phase in diffractive antennas: Review, applications, new results", *IEEE Antennas and Propagation Magazine*, vol. 53, no. 2, pp. 77–94, Apr. 2011, ISSN: 1045-9243.

[24] "Iso 14644-1: cleanrooms and associated controlled environments — part 1", International Organization for Standardization, Geneva, CH, Tech. Rep., Dec. 2015.

[25] M. A. Mohammad, M. Muhammad, S. K. Dew, and M. Stepanova, "Fundamentals of electron beam exposure and development", in *Nanofabrication: Techniques and Principles*. Vienna: Springer Vienna, 2012, pp. 11–41, ISBN: 978-3-7091-0424-8.

[26] M. Hatzakis, "Electron resists for microcircuit and mask production", *Journal of The Electrochemical Society*, vol. 116, no. 7, pp. 1033–1037, 1969.

[27] M. Aktary, M. Stepanova, and S. K. Dew, "Simulation of the spatial distribution and molecular weight of polymethylmethacrylate fragments in electron beam lithography exposures", *Journal of Vacuum Science & Technology B: Microelectronics and Nanometer Structures Processing, Measurement, and Phenomena*, vol. 24, no. 2, pp. 768–779, 2006.

[28] S. Ma, C. Con, M. Yavuz, and B. Cui, "Polystyrene negative resist for high-resolution electron beam lithography", *Nanoscale research letters*, vol. 6, no. 1, p. 446, 2011.

[29] M. M. Greve and B. Holst, "Optimization of an electron beam lithography instrument for fast, large area writing at 10 kv acceleration voltage", *Journal of Vacuum Science & Technology B, Nanotechnology and Microelectronics: Materials, Processing, Measurement, and Phenomena*, vol. 31, no. 4, p. 043 202, 2013.

[30] B. D. Vogt, E. K. Lin, W.-l. Wu, and C. C. White, "Effect of film thickness on the validity of the sauerbrey equation for hydrated polyelectrolyte films", *The Journal of Physical Chemistry B*, vol. 108, no. 34, pp. 12 685–12 690, 2004.

[31] N. Einspruch and D. Brown, *Plasma Processing for VLSI*, ser. VLSI Electronics Microstructure Science. Elsevier Science, 2014, ISBN: 9781483217758.

[32] K. Nojiri, "Mechanism of dry etching", in *Dry Etching Technology for Semiconductors*. Springer International Publishing, 2015, pp. 11–30, ISBN: 978-3-319-10295-5.

[33] G. Fortuño, "Study of reactive ion etching of si and sio2 for cfxcl4-x gases", *Plasma Chemistry and Plasma Processing*, vol. 8, no. 1, pp. 19–34, Mar. 1988, ISSN: 1572-8986.

[34] H. Park, C. Garvin, D. Grimard, and J. Grizzle, "Control of ion energy in a capacitively coupled reactive ion etcher", *Journal of the Electrochemical Society*, vol. 145, no. 12, pp. 4247–4252, 1998.

[35] R. J. Gillespie, "Covalent and ionic molecules: Why are bef2 and alf3 high melting point solids whereas bf3 and sif4 are gases?", *Journal of Chemical Education*, vol. 75, no. 7, p. 923, 1998.

[36] P. Vanysek, "Electrochemical series", in *CRC Handbook of Chemistry and Physics*, D. R. Lide, Ed., 83rd ed. CRC Press: Boca Raton, 2002, pp. 8-21–8-31.

[37] C. Vargel, *Corrosion of Aluminium*. Elsevier Science, 2004, pp. 81–111, ISBN: 9780080472362.

[38] S. Franssila, *Introduction to Microfabrication*. Wiley, 2010, ISBN: 9781119991892.

[39] K. Sato, M. Shikida, Y. Matsushima, T. Yamashiro, K. Asaumi, Y. Iriye, and M. Yamamoto, "Characterization of orientation-dependent etching properties of single-crystal silicon: Effects of koh concentration", *Sensors and Actuators A: Physical*, vol. 64, no. 1, pp. 87–93, 1998, ISSN: 0924-4247.

[40] J. M. Łysko, "Anisotropic etching of the silicon crystal-surface free energy model", *Materials Science in Semiconductor Processing*, vol. 6, no. 4, pp. 235–241, 2003, ISSN: 1369-8001.

[41] E. van Veenendaal, A. Nijdam, J. van Suchtelen, K. Sato, J. Gardeniers, W. van Enckevort, and M. Elwenspoek, "Simulation of anisotropic wet chemical etching using a physical model", *Sensors and Actuators A: Physical*, vol. 84, no. 3, pp. 324–329, 2000, ISSN: 0924-4247.

[42] H. Seidel, L. Csepregi, A. Heuberger, and H. Baumgärtel, "Anisotropic etching of crystalline silicon in alkaline solutions: I . orientation dependence and behavior of passivation layers", *Journal of The Electrochemical Society*, vol. 137, no. 11, pp. 3612–3626, 1990.

[43] K. Biswas and S. Kal, "Etch characteristics of koh, tmah and dual doped tmah for bulk micromachining of silicon", *Microelectronics Journal*, vol. 37, no. 6, pp. 519–525, 2006, ISSN: 0026-2692.

[44] R. Reichelt, "Scanning electron microscopy", in *Science of Microscopy*, P. W. Hawkes and J. C. H. Spence, Eds. New York, NY: Springer New York, 2007, pp. 133–272, ISBN: 978-0-387-49762-4.

[45] B. Wu and A. R. Neureuther, "Energy deposition and transfer in electron-beam lithography", *Journal of Vacuum Science & Technology B: Microelectronics and Nanometer Structures Processing, Measurement, and Phenomena*, vol. 19, no. 6, pp. 2508–2511, 2001.

[46] M. M. Greve, A. M. Vial, J. J. Stamnes, and B. Holst, "The beynon gabor zone plate: A new tool for de broglie matter waves and hard x-rays? an off axis and focus intensity investigation", *Opt. Express*, vol. 21, no. 23, pp. 28 483–28 495, Nov. 2013.

[47] T. A. Green, "Gold etching for microfabrication", *Gold Bulletin*, vol. 47, no. 3, pp. 205–216, Sep. 2014, ISSN: 2190-7579.

[48] T. Y. Kang, G. Kim, I. H. Cho, D. Seo, and S. J. Hong, "Process optimization of cf 4/ar plasma etching of au using i-optimal design", *Thin Solid Films*, vol. 517, no. 14, pp. 3919–3922, 2009.

[49] *Corrosion resistance of the austenitic chromium-nickel stainless steels in chemical environments*, One New York Plaza, New York, N.Y. 10004, 1963.

[50] R. Wüest, P. Strasser, F. Robin, D. Erni, and H. Jäckel, "Fabrication of a hard mask for inp based photonic crystals: Increasing the plasma-etch selectivity of poly(methyl methacrylate) versus sio2 and sinx", *Journal of Vacuum Science & Technology B: Microelectronics and Nanometer Structures Processing, Measurement, and Phenomena*, vol. 23, no. 6, pp. 3197–3201, 2005.

[51] R. J. Visser, "Determination of the power and current densities in argon and oxygen plasmas by in situ temperature measurements", *Journal of Vacuum Science & Technology A: Vacuum, Surfaces, and Films*, vol. 7, no. 2, pp. 189–194, 1989.

[52] B. C. Dems and F. Rodriguez, "The role of heat transfer during reactive-ion etching of polymer films", *Journal of Vacuum Science & Technology B: Microelectronics Processing and Phenomena*, vol. 8, no. 6, pp. 1985–1989, 1990.

[53] N. Rueger, M. Doemling, M. Schaepkens, J. Beulens, T. Standaert, and G. Oehrlein, "Selective etching of sio2 over polycrystalline silicon using chf3 in an inductively coupled plasma reactor", *Journal of Vacuum Science & Technology A: Vacuum, Surfaces, and Films*, vol. 17, no. 5, pp. 2492–2502, 1999.

[54] P. French, P. Sarro, R. Mallée, E. Fakkeldij, and R. Wolffenbuttel, "Optimization of a low-stress silicon nitride process for surface-micromachining applications", *Sensors and Actuators A: Physical*, vol. 58, no. 2, pp. 149–157, 1997, ISSN: 0924-4247.

[55] C. B. Nielsen, C. Christensen, C. Pedersen, and E. V. Thomsen, "Particle precipitation in connection with koh etching of silicon", *Journal of The Electrochemical Society*, vol. 151, no. 5, G338–G342, 2004.

[56] Z. Zhu and C. Liu, "Simulation of anisotropic crystalline etching using a continuous cellular automata algorithm", *CMES-Computer Modeling in Engineering & Sciences*, vol. 1, no. 1, pp. 11–19, 2000.

[57] G. Scotti, P. Kanninen, T. Kallio, and S. Franssila, "Bulk-aluminum microfabrication for micro fuel cells", *Journal of Microelectromechanical Systems*, vol. 23, no. 2, pp. 372–379, Apr. 2014, ISSN: 1057-7157.

[58] J. Fan, W. T. Zhang, J. Q. Liu, W. J. Wu, T. Zhu, and L. C. Tu, "Fabrication of high aspect ratio structure and its releasing for silicon on insulator mems/moems device application", *Journal of Micro/Nanolithography, MEMS, and MOEMS*, vol. 14, no. 2, p. 024 502, 2015.

[59] W. Chao, J. Kim, S. Rekawa, P. Fischer, and E. H. Anderson, "Demonstration of 12 nm resolution fresnel zone plate lens based soft x-ray microscopy", *Opt. Express*, vol. 17, no. 20, pp. 17 669–17 677, Sep. 2009.

Appendix

Python script for creating support pattern

```
from math import *

def t_factor(t):
    '''
    Takes in final membrane thickness, returns total
    extra width needed per zone
    '''
    x=t/sqrt(2)
    return 2*x

def zone_change(data, output_file, thickness, vertices):
    """
    Reads a line from the data and writes the revised
    zone widths to the output file.
    """
    zones=[["Middle", "Inner", "Outer"]]
    for iteration, line in enumerate(data):
        row=line.split(" ")
        if row[0]=="C":
            width_old=float(row[3])
            width_new=width_old+t_factor(thickness)
            new_row="{0} {1} {2} {3:.14f}".format(
            row[0],row[1],row[2], width_new)
            output_file.write("{0}\n".format(new_row))
        elif (iteration-2)%5==0:
            radius=float(row[0])
            zones.append([radius,radius-(width_new/2),
                          radius+(width_new/2)])
            output_file.write("{0}".format(line))
        elif (iteration-3)%5==0:
            output_file.write("{0}\n".format(vertices))
        else:
```

```
33              output_file.write("{0}".format(line))
34      return zones
35
36  def central_stop(zones, output_file, stop_size,vertices):
37      """
38      Finds the closest zone to the desired central
39      stop diameter and sets the diameter to the
40      inner part of first zone encountered.
41      """
42      for triple in zones[1:]:
43          inner=triple[1]
44          if inner>stop_size*500:
45              stop_size=inner/500
46              break
47
48      print("Central stop with diameter {0:.4f} mm in layer 1".
49            format(stop_size))
50      output_file.write("C 100.0 1\n0.000 0.000\n{0}\n{1}\n#\n".
51                        format(stop_size*500,vertices))
52      #For the combined layer
53      output_file.write("C 100.0 4\n0.000 0.000\n{0}\n{1}\n#\n".
54                        format(stop_size*500,vertices))
55
56  def second_support(data, thickness, stop_size, file_out, bar_radius,bar_
57      """
58      Writes the main support bars to the output file and
59      adds a new set of support bars, bisecting the previous
60      set whenever length/width exceeds the factor. The set of
61      secondary support bars is then written to the output file.
62      """
63
64      #16 main bars every 22.5 deg
65      angles=[0.1*x*pi/180 for x in range(0,1800,225)]
66      x_list=[bar_radius*x for x in [-1,-1,1,1,-1]]
67      y_list=[bar_width/2*x for x in [-1,1,1,-1,-1]]
68      #Write elements, rotating around center
69      for angle in angles:
70          file_out.write("1 100.0 2\n")
71          for i,element in enumerate(x_list):
72              x=x_list[i]*cos(angle)-y_list[i]*sin(angle)
73              y=x_list[i]*sin(angle)+y_list[i]*cos(angle)
74              file_out.write("{0} {1}\n".format(x,y))
75          file_out.write("#\n")
```

```
76      #For the combined layer:
77      for angle in angles:
78          file_out.write("1 100.0 4\n")
79          for i,element in enumerate(x_list):
80              x=x_list[i]*cos(angle)-y_list[i]*sin(angle)
81              y=x_list[i]*sin(angle)+y_list[i]*cos(angle)
82              file_out.write("{0} {1}\n".format(x,y))
83          file_out.write("#\n")
84      #Sectors divided by bars:
85      sectors=16
86      for iteration, line in enumerate(data):
87          row=line.split(" ")
88          if row[0]=="C":
89              width=float(row[3])+t_factor(thickness)
90              width_closed=float(row[3])-t_factor(thickness)
91              #Subtracts t_factor to give the approximate width
92              #of the zones that is not written
93              #This will be the width of the nitride
94          elif (iteration-2)%5==0:
95              radius=float(row[0])
96              if radius>stop_size*500:
97                  criterion=pi*2*radius/sectors*(1/width_closed)
98                  if criterion>factor:
99                      new_support=radius-(width/2)-0.25
100                     #Subtract 250nm to make sure we cover whole zone
101                     sectors=sectors*2
102                     angles=[]
103                     for x in range(0,(sectors+1)/2):
104                         angles.append(2*pi/sectors*(1+2*x))
105                     x_list=[new_support,new_support,
106                             bar_radius,bar_radius,new_support]
107                     y_list=[bar_width/2*x for x in [-1,1,1,-1,-1]]
108                     for angle in angles:
109                         file_out.write("1 100.0 2\n")
110                         for i,element in enumerate(x_list):
111                             x=x_list[i]*cos(angle)-y_list[i]*sin(angle)
112                             y=x_list[i]*sin(angle)+y_list[i]*cos(angle)
113                             file_out.write("{0} {1}\n".
114                                            format(x,y))
115                         file_out.write("#\n")
116
117                     #For the combined layer:
118                     file_out.write("1 100.0 4\n")
```

```
119                             for i,element in enumerate(x_list):
120                                 x=x_list[i]*cos(angle)-y_list[i]*sin(angle)
121                                 y=x_list[i]*sin(angle)+y_list[i]*cos(angle)
122                                 file_out.write("{0} {1}\n".
123                                                format(x,y))
124                             file_out.write("#\n")
125     print("{0} um support bars in layer 2.".format(bar_width))
126
127 def arcs(file_out, vertices,bar_radius,rotation):
128     """
129     Writes arc from 1/8 to 3/8, 5/8 to 7/8, 9/8 to 11/8,
130     13/8 to 15/8. All in pi radians.
131     """
132     start=0
133     if rotation=="y":
134         start=45
135     for x in range(4):
136         file_out.write("A 100.0 3\n0.000 0.000\n")
137         file_out.write("{0}\n{1}\n".
138                        format(bar_radius,vertices))
139         file_out.write("{0} 22.500 67.500\n#\n".
140                        format(start+90*x))
141
142         #For the combined layer:
143         file_out.write("A 100.0 4\n0.000 0.000\n")
144         file_out.write("{0}\n{1}\n".
145                        format(bar_radius,vertices))
146         file_out.write("{0} 22.500 67.500\n#\n".
147                        format(start+90*x))
148     print("Arcs to block diagonals in layer 3.")
149
150
151 def main():
152     '''
153     Inputs textfile .asc of zoneplate, corrects it
154     into a second file with added widths for zones
155     '''
156     name=raw_input("Input filename: ")
157     thickness=float(input("Input final thickness of substrate [um]: "))
158     c_stop=raw_input("Do you want a central stop? y/n: ")
159     stop_size=0
160     if c_stop=="y":
161         stop_size=input("Diameter of central stop [mm]: ")
```

```
162     support=raw_input("Do you want support bars? y/n: ")
163     rotation=raw_input("Do you want 45 deg rotation on arcs? y/n: ")
164     vertices=1024
165     print("Opening {0}...".format(name))
166     file_1=open(name,"r")
167     name_core=name.split(".asc")
168     file_out=open("{0}_new.asc".format(name_core[0]), "w")
169     data=file_1.readlines()
170     zones=zone_change(data, file_out, thickness, vertices)
171 
172     if c_stop=="y":
173         central_stop(zones, file_out, stop_size, vertices)
174 
175     if support=="y":
176         bar_width=50
177         factor=input("What do you want the l/w factor to be: ")
178         #Will write new set of support bars when length/width > factor
179 
180         #Find radius outer ring for support bar endpoint
181         outer_radius=eval(data[len(data)-3])
182         outer_width=eval(data[len(data)-5].split(" ")[3])
183         bar_radius=outer_radius+outer_width+50
184         #50um factor to secure overshot
185 
186 
187         second_support(data, thickness, stop_size, file_out,
188                        bar_radius, bar_width, factor)
189     arcs(file_out, vertices, bar_radius, rotation)
190     print("Copy of all items to be removed gathered in layer 4.")
191 
192 
193     file_1.close()
194     file_out.close()
195     print("Done.")
196 
197 main()
```